Permanent Magnet Synchronous Machine Rotor Vibration Measurement System

by

María Martínez Gómez
uo224394@uniovi.es

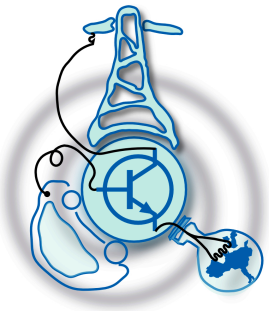

Submitted to the Department of Electrical Engineering, Electronics, Computers and Systems
in partial fulfillment of the requirements for the degree of
Master of Science in Electrical Energy Conversion and Power Systems
at the
UNIVERSIDAD DE OVIEDO
July 2017

Author .....

Certified by .....
David Díaz Reigosa
Associate Professor
Thesis Supervisor

Certified by .....
Daniel Fernández Alonso
Dr.
Thesis Supervisor

Permanent Magnet Synchronous Machine Rotor Vibration Measurement System

by

María Martínez Gómez

uo224394@uniovi.es

Submitted to the Department of Electrical Engineering, Electronics, Computers and Systems
on July 14, 2017, in partial fulfillment of the
requirements for the degree of
Master of Science in Electrical Energy Conversion and Power Systems

Abstract

Minimization of torque pulsation in Permanent Magnet Synchronous Machines has been the focus of significant research efforts during the last decades. However, accurate measurement systems able to monitor torque pulsation at the rotor shaft have not been developed so far. In this master thesis, a rotor vibration measurement system with an innovative on-line monitoring method is developed. The measurements obtained from the designed prototype will be validated through Finite Element Analysis of the real machine. Finally, in order to produce a smoother output torque, a harmonic compensation strategy has been developed and implemented in Simulink.

Keywords Permanent magnet synchronous machines, torque ripple, cogging torque, reluctance torque, Phase Locked Loop, harmonic compensation.

Thesis Supervisor: David Díaz Reigosa
Title: Associate Professor

Thesis Supervisor: Daniel Fernández Alonso
Title: Dr.

Acknowledgments

En primer lugar me gustaría agradecer a mi tutor de tesis, David Díaz Reigosa, su gran apoyo y paciencia durante la realización de esta tesis. Gracias por guiarme en esta andadura, y por tu gran conocimiento que sin duda ha sido clave para lograr el resultado de este experimento.

En segundo lugar, agradecir a mi co-tutor de tesis, Daniel Fernandez, sus consejos, brillantes ideas y, su manera de hacerme ver fácil lo que hasta hace poco veía imposible.

Agradecer la ayuda recibida para la realización de este Trabajo Fin de Master a Thyssenkrupp que, mediente la concesión de una ayuda económica, ha financiado integramente este proyecto. La adjudicación de dicha ayuda se encuentra en el marco de la Cátedra de Movilidad de la Universidad de Oviedo financiada por la empresa Thyssenkrupp, cuya referencia de la FUO es CAT-003-17.

Aprovecho esta sección para agradecer a mis amigas su capacidad única de hacerme evadirme del mundo. Y, por supuesto, no puedo olvidarme de mis compañeros del master, porque realmente empezamos como tal pero después de estos dos años, más que compañeros les puedo llamar amigos. Gracias por haber hecho de estos dos años, algo para recordar de una manera alegre y divertida. No puedo imaginar mejor compañeros de batalla.

Mención especial se merece Lino. Gracias por haberme acompañado durante este largo proceso, por enseñarme a ver con perspectiva y apoyarme en cada desisión tomada, aunque eso haya significado dejar muchas cosas en un segundo plano. Todo hubiese sido mucho más cuesta arriba sin ti.

Por último, pero no menos importante, agradecer a mis padres su apoyo incondicional e infinita paciencia. No os podría agradecer lo suficiente todas las oportunides que me dais. Estas ultimas palabras de agradecimiento van dedicadas a mis abuelos, gracias por los valores de vida que me habeis enseñado y vuestra manera única de hacerme sentir especial. Siempre os querré.

Contents

List of Figures

List of Tables

Table of Symbols

Subscripts

r	rotor
s	stator
dq	dq reference frame component
e	electrical
m	mechanical
c	centripetal
t	tangential
pu	per unit value
0	DC magnitude
n	harmonic number

Superscripts

r	rotor synchronous reference frame
hf	harmonic synchronous reference frame
$*$	Reference/command value
$\widehat{\ }$	Estimated value

Acronyms

PMSM	Permanent Magnet Synchronous Machine
IPMSM	Interior Permanent Magnet Synchronous Machine
SPMSM	Surface Permanent Magnet Synchronous Machine
FDD	Fault Detection and Diagnosis
MCSA	Motor Current Signature Analysis
FEA	Finite Element Analysis
FEM	Finite Element Method
PCB	Printed Circuit Board
PM	Permanent Magnet
MMF	Magnetomotive Force
EMF	Electromagnetic Force
LCM	Least Common Multiple
FFT	Fast Fourier Transform
ODR	Output Data Rate
MEMS	Micro Electro-Mechanical Systems
DC	Direct Current
PLL	Phase Locked Loop
HPF	High-Pass Filter
LPF	Low-Pass Filter
BSF	Band-Stop Filter
PI	Proportional-Integral
PR	Proportional-Resonant

Variables

a	linear acceleration
b	friction coefficient
d	shaft diameter
F	force
f	frequency
h	harmonic order
i	current
J	inertia coefficient
j	imaginary unit
K_i	integral controller gain
K_p	proportional controller gain
L	inductance
λ	flux linkage
m	mass
N	number of coils
ω	angular speed
α	angular acceleration
μ	permeability
p	pole pairs
Φ	magnetic flux
R	electric resistance
$\Re$	magnetic reluctance

r radius

T torque

t time

θ angular position

ϕ phase shift

P active power

Q number of stator slots

v voltage

Chapter 1

Introduction

In the last decades, design and control of Permanent Magnet Synchronous Machines (PMSMs) has been the focus of significant research efforts due to their superior performance in key aspects as efficiency, power density, and dynamic response when compared to other machine types. These features have made PMSMs inherent suitability in many applications such as automotive, robotics, servo drive systems, military, or aerospace applications, etc.

However, PMSMs are less robust compared to other types of machines drives such as induction machines because of the inherent demagnetization risk of the permanent magnets. This becomes an important drawback in safety critical applications, in which failures cannot be tolerated.

For that reason, fault detection and diagnosis (FDD) is one of the aspects related with electrical machines that most interest is getting from industrial applications. Some techniques have been widely investigated to be applied in certain applications where the reliability of the systems must be ensured. The most relevant ones are the motor current signature analysis (MCSA), vibration measurement systems or artificial Intelligence (AI) techniques [1].

Among the above mentioned techniques, vibration measurement systems has experienced a sustained growth in industrial applications because of the potential on detecting abnormal performance of the machine at earlier stages of a fault and thus, allowing to adapt the control and reduce the risk of a catastrophic failure.

Another inherent issue in PMSMs that cannot be tolerable for high precision applications such as laser cutting, robotics or arc welding, is the manifestation of periodic torque fluctuations at the rotor shaft. Significant effort has been putted during the last 30 years for torque ripple minimization through current-based techniques or motor design optimization. However, accurate measurements for not-current dependent fluctuations, commonly known as cogging torque, has not been addressed so far, except by the placement of expensive torque sensors at the rotor shaft. So that developing a vibration monitoring system that could be integrated within the machine control strategy with the aim of minimizing the risk of electrical machine drive failures but also with the goal of monitoring torque ripple and cogging torque of PMSMs, is a challenge nowadays.

The aim of this thesis is to design a vibration monitoring system in order to address torque ripple and cogging torque measurements of a PMSM. Torque pulsations will appear as a consequence of the non-uniformity design of the machine. Thus, by a careful control design, torque fluctuations could be reduced. As a consequence of producing smoother torque, mechanical faults such as bearing faults, gearbox faults, etc. will be substantially diminish.

Chapter 2

Objectives of the Master Thesis

As it has been mentioned in Chapter 1, this thesis will be focused on the design and development of a vibration measurement system in order to monitor torque pulsations at the rotor shaft of a PMSM. This objective will be covered following different tasks:

- Brief review of previous work on different techniques to measure or estimate torque ripple and cogging torque: Study and brief analysis of the major advantages and drawbacks of the methods already published on the topic. An innovative method will be proposed in this thesis as an alternative to these techniques.

- Theoretical model of the PMSMs: A mathematical model including a deeply explanation of cogging torque and torque ripple of the machine will be developed in order to understand the working principle of the machine.

- Finite element analysis of the machine: The use of simulation software allows validating and improving the results obtained from the theoretical models. Finite element analysis will allow analysing separately the effect of each motor design element (size, winding configuration, magnets configuration,...) have over the torque oscillation. This study is not possible to be done experimentally due to the unaffordable cost of constructing a large number of motor configurations.

- Design and development of the rotor vibration measurement system: A vibra-

tion measurement system to obtain on-line measurements of the tangential and radial acceleration of the machine rotor shaft will be developed. A PCB containing a 3-axis accelerometer will be attached to the shaft of the machine. The measurements will be transmitted through a Wi-Fi link to a designed application in the software Builder C_{++} for data acquisition.

- Experimental results: Data obtained from the vibration measurement system will be processed to extract the information related with torque ripple and cogging torque. The experimental data from the vibration measurement system will be validated comparing the experimental results with FEM simulations.

- Torque harmonic compensation: At the last point, a control strategy for torque harmonics compensation will be proposed for future implementation in the machine control.

Chapter 3

State of the Art

This chapter covers the state of art in modelling of torque pulsation of permanent-magnet synchronous machine (PMSM) drives. First, both the electrical and mechanical mathematical models of the machine are presented. Later, a study of types of torque pulsation is developed. Since cogging torque has proven to be, among the types of torque ripple, one of the most difficult to be measured, a deeper study of it has been done. Finally, different methods already published to measure cogging torque and torque ripple are reviewed with the main advantages, drawbacks and limitations.

3.1 Permanent Magnet Synchronous Machines

PMSMs can be broadly classified into three categories depending on the magnet position [1]: Interior Permanent Magnet (IPM) motors which permanent magnets are mounted inside the cylindrical rotor, Surface Permanent Magnet (SPM) motors which permanent magnets are placed on its surface or, Inset PM machines which magnets are embedded inside hollows on the rotor surface. Because of mounting the PMs on the rotor surface, SPMSMs are non-salient machines ($\mu_{magnet} \approx \mu_{air}$). This implies that the inductance variation with rotor position can be negligible. On the contrary, the iron between the permanent magnets in IPM or Inset PM machines creates a saliency ($\mu_{magnet} \neq \mu_{iron}$), leading an inductance variation with rotor position and the manifestation of torque pulsations as the shaft rotates.

3.1.1 Electrical Model

The electrical model of a PMSM in the dq-rotor synchronous reference with no rotor cage is described by equations (3.1) to (3.4) [2].

$$v_d^r = R_s i_d^r + \frac{d}{dt}\lambda_{ds}^r - \omega_r \lambda_{qs}^r \tag{3.1}$$

$$v_q^r = R_s i_q^r + \omega_r \lambda_{ds}^r + \frac{d}{dt}\lambda_{qs}^r + \omega_r \lambda_{PM} \tag{3.2}$$

$$\lambda_{ds}^r = L_{ds} i_d^r \tag{3.3}$$

$$\lambda_{qs}^r = L_{qs} i_q^r \tag{3.4}$$

Where v_{dq}^r are the voltages across the dq-stator winding and, λ_{dqs}^r the dq-stator flux linkages.

The electromagnetic torque of a PM synchronous machine can be defined as

$$T_e = \frac{3p}{2}((\lambda_{ds}^r + \lambda_{PM}) i_q^r - \lambda_{qs}^r i_d^r) \tag{3.5}$$

Where p is the number of poles pairs of the machine. Torque equation can be expanded by simply substitution of (3.3) and (3.4) in (3.5).

$$T_e = \frac{3p}{2}\left[\lambda_{PM} i_q^r + (L_{ds} - L_{qs}) i_d^r i_q^r\right] \tag{3.6}$$

The first term of (3.6) is the mutual torque produced by the interaction between the PM magnetic field with the electromagnets on the stator. Since the mutual torque is the cause because the rotor shaft turns, it is considered to be beneficial to the performance of PMSM. The second term which is proportional to the magnetic anisotropy of the machine is commonly known as reluctance torque. As it has been seen, SPMSMs will exhibit almost zero reluctance torque since d-axis inductance is nearly the same than q-axis value. On the contrary, IPMSMs and Inset PMM will suffer of higher torque pulsation due to the inductance variation with rotor position.

3.1.2 Mechanical model

Since the dynamics of the rotating PMSM's shaft and its load can be liken as a mass-damper system, mechanical torque can be expressed by (3.9) [3].

$$T_m = J\alpha_m + b\omega_m \tag{3.7}$$

being α_m the mechanical angular acceleration, ω_m the mechanical angular speed, J and b the inertia and friction coefficients, respectively.

It will be useful for the understanding of this project to relate mechanical and electrical position or speeds. Mechanical speed can be defined as the speed of the motor shaft, while a complete electrical cycle can be defined as the mechanical rotor movement needed to put the rotor in an identical magnetic orientation. This relationship can be defined as [4]

$$\omega_e = p\omega_m \tag{3.8}$$

As (3.8) shows, mechanical and electrical variables can be related with the number of pole pairs.

3.2 Sources of torque oscillation

With an ideal design, PMSMs would develop a constant output torque without oscillations. Torque ripple can be neglected if winding distribution and feeding currents were perfectly sinusoidal. However, the slot opening will create a reluctance variation, being the cause of another type of torque oscillation, commonly known as cogging torque. There are mainly three types of periodic torque fluctuation sources [4–6]

- **Mutual torque** will be created by the interaction of the permanent magnets of the rotor with the opposite electromagnets of the stator. These electromagnets are created due to the current flow through the stator coils. Torque ripple will appear either if rotor's magnetic field or stator's current waveform are not perfectly aligned or any waveform is not pure sinusoidal with equal amplitude.

- **Reluctance torque** will appear in PMSMs when the winding inductance varies with the rotor position because of the machine saliency. Reluctance torque is proportional to the square of the current but it will be almost negligible for SPM machines.

- **Cogging torque**, also called detent torque, will appear in the rotor shaft due to the interaction between the rotor's PM and the stator slots. Cogging torque will appear when the shaft rotates even when there is no current flow, therefore it can not be directly measured using current sensors. This torque could only be eliminated if slots were completely closed, but this is not feasible in practice.

Following the conservation of energy principle and considering the electrical machine a conservative system where no energy is lost, the above mentioned torque components can be mathematically modelled from a macroscopic viewpoint [4] .

$$T = \frac{1}{2} i^2 \frac{dL}{d\theta} - \frac{1}{2} \Phi^2 \frac{d\Re}{d\theta} + Ni \frac{d\Phi}{d\theta} \tag{3.9}$$

The first term describes the reluctance torque while the second term characterizes the cogging torque that will appear whenever the flux leaving the magnets travels through a varying reluctance. The negative sign represents the inverse proportionality between the inductance and the reluctance. The third term describes the mutual torque. Mutual torque can be defined as the mutual flux Φ linking the magnet to the coil. Mismatches between the flux leaving the magnets and the current through the stator coil will lead to torque ripple.

3.2.1 Torque ripple

High frequency torque ripple will appear in PMSMs whenever the back electromotive force (EMF) or feeding currents deviate from their ideal characteristics. Since the magnetic field is not perfectly sinusoidal, high order harmonics will appear in the induced EMF's force. Feeding currents will also contain high order harmonics because of the inverter dead-time and anomalies in the operation of the PMSMs. However,

since both waveforms will be half-wave symmetric, all even harmonics will be zero. Thus, for three-phase machines, torque ripple will arise at frequencies equal to six times the fundamental frequency. As a result, the mutual torque shown in (3.9) can be rewritten as a sum of the average component and multiples of six order harmonics. [7]

$$T = T_0 + \sum_{n=1}^{\inf} T_{6n} \cdot cos(n6wt + \phi_{6n}) \tag{3.10}$$

where T_0 is the average mutual torque and T_{6n} are the torque ripple harmonic components.

Since PMSMs can be feeded with any arbitrary current shape, many researches have been focused on the torque ripple elimination by the proper injection of feeding current harmonics [4, 7, 8].

3.2.2 Cogging torque

Many studies have point out the influence of the number of slots/poles of a PMSM to the cogging torque waveform. The period of the cogging torque will be determined by the least common multiple LCM between the number of slots and poles of an electric machine. Being Q the number of slots of a PMSM, the number of cogging torque periods N_{cog} per revolution will be given by (3.11) [6, 9, 10].

$$N_{cog} = LCM(Q, 2p) \tag{3.11}$$

E.g. For a 36slots/6poles PMSM, which least common multiple is 36, the cogging period will be 360 mechanical degrees by 36, which in this case leads to 10 mechanical degrees. Thus, in a complete turn of the motor shaft, 36 cogging torque periodicities will appear at the generated output torque.

Increasing the number of slots and poles of the machine will increase the cogging torque harmonic frequency but also reduce the amplitude of the cogging torque waveform, being easier to be filtered by the load inertia. This could be the first approach to achieve a smoother torque. Other design aspects such as pole shoe shaping, air gap

length widening, fractional slots configuration or skewing the stator, are commonly adopted to reduce cogging torque. However, these advanced designing techniques will increase the manufacturing cost and decrease the whole performance of the machine. For that reason, designing an accurate vibration measurement system able to give information of cogging torque for machine characterization is a challenge that industry faces nowadays [10].

3.3 Cogging torque and Torque ripple measurement techniques

Despite the significant effort that research community has been putted on torque oscillation minimization through mechanical design optimization or carefully control systems, accurate measurement systems able to measure torque pulsation at the rotor shaft have not been developed so far. From the literature, some prototypes recently proposed are explained below:

- Motor current signature analysis (MCSA) technique has been widely applied for diagnosis of electrical machines because it is a non-intrusive method, so it does not disturb the normal performance of the machine. This method is based on the Fast Fourier Transform (FFT) analysis of the line currents. The drawback is that current spectrum distorts under speed oscillations. In addition, this technique is not suitable for measuring cogging torque since it is not directly dependent on the stator current [1, 11].

- A simple method for measuring cogging torque has been proposed in [12]. The prototype is fixed to the stator with a chuck of lathe to measure its reaction torque. A balanced beam attached to the rotor shaft will have one extreme placed on top of a digital weight gauge in order to monitor the variation on weight when the lathe rotates. This variation will reflect the variation of cogging torque at each rotor position. The drawback of this method is that zero/low

speeds measurements have to be done, thus only cogging torque can be measured.

- Mechanical sensors such as force sensors or torque sensors are used as a solution for measuring all types of torque pulsation. However, torque sensors are a source of flexible coupling that could introduce resonant oscillations to the system and mask the actual vibration of the shaft. In addition, these mechanical sensors could be more costly that the machine itself [13–15].

- Monitoring position errors at the position/speed control is an alternative technique proposed in [5] to monitor acceleration changes. Through this technique it is possible to detect torque ripple without measuring torque directly, thus no extra sensors will be needed. The drawback of this technique is that high-frequency speed variations cannot be accurately tracked. This is because the bandwidth of a closed-loop position control is not fast enough to follow high frequency disturbances.

As it has been seen, torque fluctuation will appear at the output shaft creating speed fluctuation, audibly noise and vibration. At high speeds, vibration will be masked by the rotor inertia but at low speed ranges, torque pulsation can cause large speed fluctuations that will be directly reflected in shaft vibrations. Measurement of the rotor movement to detect torque pulsations without affecting the motor dynamics will be the goal of this Master Thesis.

Chapter 4

Rotor Vibration Measurement System

On previous researches different prototypes have been focused on measuring dynamic torque fluctuations from the rotating shaft. As stated in the previous chapter, mechanical sensors such as torque transducers are one of the most suitable options to measure any type of torque fluctuations. However, these sensors have to be carefully placed to not affect the motor dynamics. In the present chapter, the experimental setup for measuring rotor vibration in PMSMs is presented. The principle of operation and system requirements for an accurate design according to the machine characterization are stated.

4.1 Principle of operation

Despite the torque definition given by (3.6) and (3.9), torque can be defined in a more general way as the product of a tangential force and the distance at which it is applied [4].

$$T = Frsin(\varphi) \tag{4.1}$$

where φ is the angle between the applied force and the radial direction ($F_t = Fsin(\varphi)$).

According to the Newton's Second Law of Motion, *"when a resultant force is ap-*

plied to a body it produces an acceleration that is directly proportional to the resultant force and inversely proportional to the mass of the body." Thus, equation (4.1) can be rewritten as shows (4.2).

$$T = ma_t r \tag{4.2}$$

Where a_t is the tangential linear acceleration and, m the mass of the body.

From (4.2) it can be seen from an intuitive viewpoint that high frequency torque harmonics will result in analogous harmonics of the tangential acceleration. However, measuring tangential acceleration without affecting the motor dynamics is a complicated task since the shaft is continuously rotating. To do so, previous prototypes have been focused on transmitting dynamic information through static measurement systems. The main goal of this thesis, as opposed to previous proposals, is to design a synchronous prototype with the rotor shaft so that on-line rotor vibrations can be measured and transmitted through a Wi-Fi link to an external application. Therefore, a PCB including a 3-axis accelerometer will be placed on the rotating shaft.

With a 3-axis accelerometer not only tangential acceleration can be measured but also radial acceleration, known as centripetal acceleration. Thus, applying the Newton's Second Law of Motion to the centripetal force, angular speed can be directly obtained. The result is shown in (4.3).

$$Fc = m\omega^2 r \longrightarrow a_c m = mw^2 r \longrightarrow a_c = \omega^2 r \tag{4.3}$$

Equation (3.9) shows that static torque is directly proportional to the angular speed of the shaft. Therefore, direct measurement of the rotor angular speed is an extra advantage of this proposal because not only dynamic torque but also static torque will be able to be monitored.

4.2 PMSM characterization

Among the PMSMs types, there are many advantages that makes IPMSMs to be a preferable choice in many industrial applications [1]:

- They are more robust at high speeds since magnets are buried inside the rotor. Thus, magnets are less susceptible to be demagnetised.
- They perform an improvement in constant power region due to their higher field weakening capability.

However, they have some shortcomings like higher assembly cost due to the difficulty to insert the magnets inside the rotor. In addition, they are more sensitive to torque pulsation as it has been seen in section 3.1. For this last reason, a three phase, 36-slot/6-pole IPMSM will be the machine used for the development of the vibration measurement system. Fig.4-1 shows the cross-section from a finite element (FE) model of the real machine which main parameters are provided in Table 4.1.

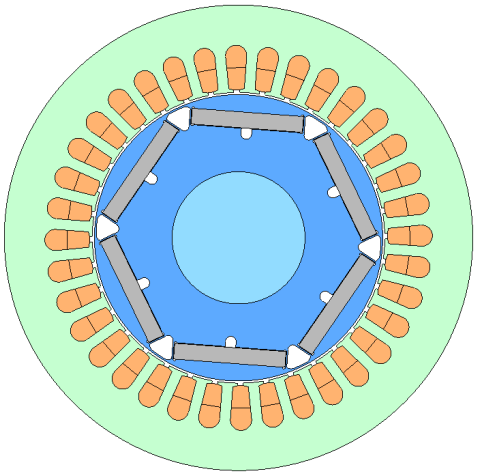

Figure 4-1: IPMSM FE model.

4.3 Prototype design

The aim of this project is to design a vibration monitoring system to rotate synchronously to the rotor shaft. Since the system will be placed on the rotor, data will not be directly accessible. For that reason, a wire-less communication interface has to be designed to receive the sampled data in an external computer. In addition, the system can neither be supplied by an external power supply. Thus, the designed prototype mainly consists of four key components: a battery, an accelerometer sensor,

Table 4.1: Three phase, 36-slot/6-pole motor parameters.

Parameters	**Symbol**	**Value**
Rated power	P_n	7.5kW
Rated voltage	V_n	350V
Pole pairs	p	3
Slot number	Q	36
Shaft outer diameter	d	40 mm
Stator resistance	R_s	0.60 Ω
Magnetizing inductance	L_m	0.03315 H
Stator leakage inductance	L_{ls}	0.0022 H
Permanent magnet flux linkage	λ_{PM}	0.176 (V·s)

a micro controller and a Wi-Fi module. A power conditioning circuit is also needed to adapt the battery voltage to the components requirements.

4.3.1 Accelerometer selection

When selecting an accelerometer sensor, some features are required like having low noise density, large sensitivity and resolution, small package and high output data rate. These characteristics are briefly discussed on the following.

- Dimensions: Since the PCB of this prototype will be placed on the rotor shaft, the diameter should be restricted to 40 mm, as shows table 4.1. This encourage the use of SMD components and the reduction of as much components as possible. Analogue Devices accelerometers' need of signal conditioning stages, increasing the number of components to measure acceleration. Therefore, micro electro-mechanical systems (MEMS) digital accelerometers seems to be the best choice for this application.

- Output Data Rate (ODR): In digital accelerometers, ODR is defined as the rate at which data is sampled. Bandwidth is defined as the highest-frequency component present in the continuous-time signal that can be reconstructed completely from the sampled signal. Thus, according to Nyquist-Shannon sampling theorem, bandwidth is specified as half the ODR value. This parameter will be

the limiting factor to measure cogging torque since it appears at high frequency order components of the fundamental rotor speed, as explained in section 3.2.2.

- Noise: Random noise at the sensor output could mask torque ripple measurements, especially high order harmonics which amplitude is usually very small [4]. In order to achieve an accurate rotor vibration measurement system, accelerometer noise density should be as low as possible. Total output noise of an accelerometer can be determined by (4.4) [16].

$$Noise = NoiseDensity\left(\frac{\mu g}{\sqrt{hz}}\right) \cdot \sqrt{1.6BW} \tag{4.4}$$

  Where BW is the accelerometer bandwidth.

- Measurement range: Torque ripple is often very small compared to mutual torque ($5\% - 10\%$). Thus, a high-full scale accelerometer able to deal with machine maximum load will not have resolution enough to provide relevant information of torque pulsation [13].

- Resolution: Resolution is a main feature when choosing the accelerometer. High bit-resolution is required for designing an accurate experimental setup.

Comparing the above mentioned characteristics among different digital accelerometers, the nano MEMS accelerometer MMA8451Q is chosen for the development of this prototype. Its main characteristics are shown in table 4.2 [17].

Table 4.2: MMA8451Q accelerometer specifications

Characteristic	**Min**	**Typ value**	**Max**	**Units**
V_{cc}	1.95	2.5	3.6	V
Noise density	99	-	126	$\frac{\mu g}{\sqrt{Hz}}$
Measurement range	-	± 2, ± 4, ± 8	-	g
Resolution	-	14	-	bits
Output Data Rate (ODR)	1.56	-	800	Hz
Package size	-	3 mm x 3 mm x 1 mm	-	mm
Operating temperature range	-40	-	85	°C

Main advantages offered by the MMA8451Q sensor compared to other sensors are: low noise density, dynamically selectable full scale, high resolution and low cost. However, it has low ODR compared with high-full scale range accelerometers. According to (3.11), cogging torque of the tested machine will appear at the 36^{th} harmonic component of the output torque. Since the bandwidth of the accelerometer is 400Hz (ODR/2), this characteristic limits the maximum operating speed of the machine to 11Hz.

4.3.2 Communication interface

Because Wi-Fi modules are mainly focus on offering very high baud rates, the communication has been established using a RN-171 Wi-Fi module. Communication using Wi-Fi modules only requires a transceiver since PCs have already integrated Wi-Fi cards.

The RN-171 Wi-Fi module is configured as a server, creating an access point with fixed IP addresses and port number. Since acceleration on the z-axis is not relevant for this application, only data from the xy-axes of the accelerometer are sent via asynchronous bus UART. In order to identify data properly, a mask must be sent before each package. This mask is selected carefully to ensure that it can never be a possible value of the data read.

It is important to note that UART serial protocol is an asynchronous serial communication in which data is not continuously synchronized by a clock signal. Synchronization has to be achieved through an start/stop bit sent before and after each byte of transmission. So, for each byte, 10 bits are sent. Therefore, three mask bytes plus two axis data with 14-bits resolution each, makes a total of 70 bits to be transmitted in each sampling interrupt. RN-171 module has to be configured with the minimum common baud rate that fulfil with data transmission requirements. The minimum baud rate needed to not lost information is given by (4.5).

$$BaudRate = \frac{80bits}{\frac{1}{800Hz}} = 53846bps \tag{4.5}$$

Thus, RN-171 module has to be configured with a baud rate equal to 115200.

4.3.3 Data acquisition

The acceleration data registers embedded inside the MMA8451Q are accessed through I^2C serial interface. Thus, the accelerometer is suitable for direct interfacing with the micro controller. In order to process and send the data to the Wi-Fi module, a PIC24FJ64GA004 micro controller is used. PIC24FJ64GA004 is a 16-bit micro controller which incorporates two independent I^2C modules, both supporting Master and Slave modes of operation and, two independent UARTs modules. Fig. 4-2 shows the algorithm designed for data acquisition.

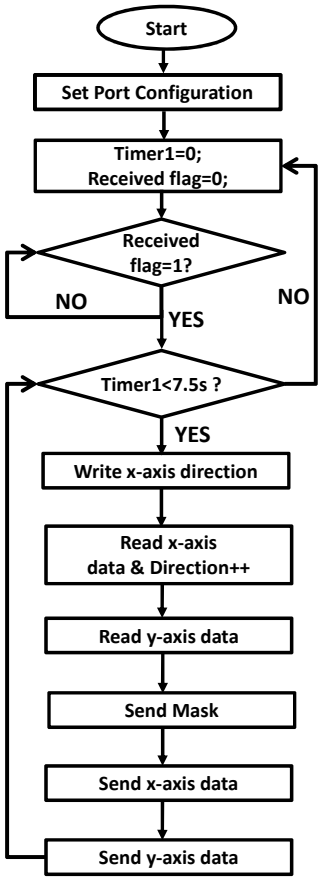

Figure 4-2: Flow chart for data acquisition

Rotor acceleration will be sampled at the maximum rate allowed by the accelerom-

eter, 800Hz. In order to receive data, a command to start sampling has to be sent through an application designed in Borland C++ Builder. From that instant, the micro-controller sends the sampled data through the Wi-Fi module to the computer during 7.5s. As stated in section 4.1, applying a FFT to the obtained acceleration data, a characterization of the output torque is achieved. Thus, 7.5s is time enough to obtain high frequency resolution.

4.3.4 Power conditioning circuit

This system will be powered by a 2-cell Li-Po battery with rated voltage of 8.4V. Thus, in order to fulfil with voltage requirements of each component, a power conditioning system is needed as shown Fig. 4-3. The value range between brackets shows the operating voltage range of each component.

A step-down TPS62056 DC/DC converter, which provides a fixed output voltage of 3.3V, is used. Main advantages offered by this synchronous step-down converter compared to others are: high efficiency and reduction of external component count due to be based on synchronous rectification with high operating frequency.

Finally, Fig. 4-4 shows the rotor vibration measurement prototype designed for this Master Thesis. A 3D printed plastic mounting has been also designed to attach the PCB on the rotor shaft. This adapter is shown in Fig. 4-5. Note that in order to avoid cross-coupling between axis measurements, x-axis of the accelerometer is carefully placed aligned with the radial direction of the rotor.

Fig. 4-6 shows a window capture of the builder application designed to receive rotor acceleration measurements. This application allows to connect with any available access point by typing the IP and Port of the server. Graphics will be updated any time new data is requested to the accelerometer. Data will be also saved in a txt file which name is defined in the application.

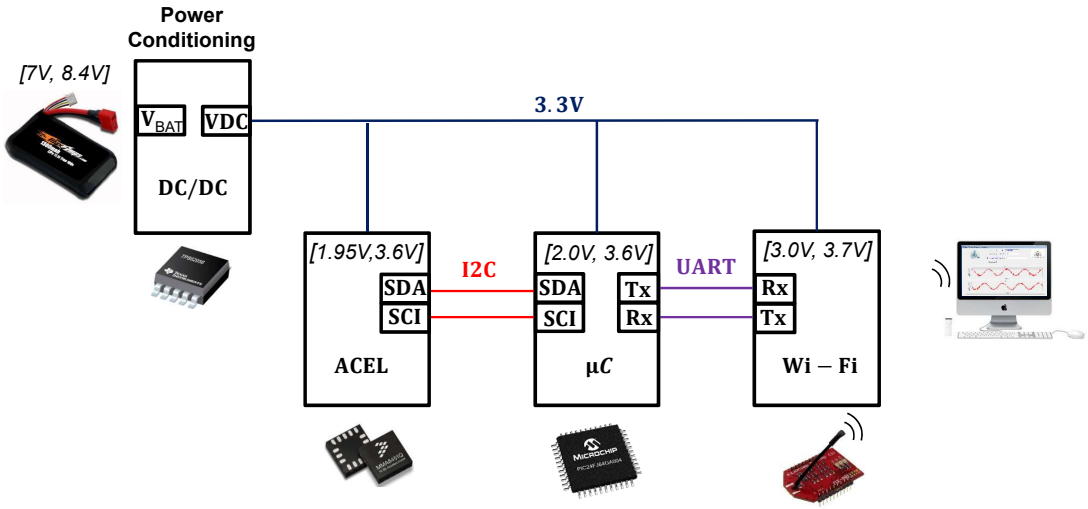

Figure 4-3: Block diagram of the power conditioning stage.

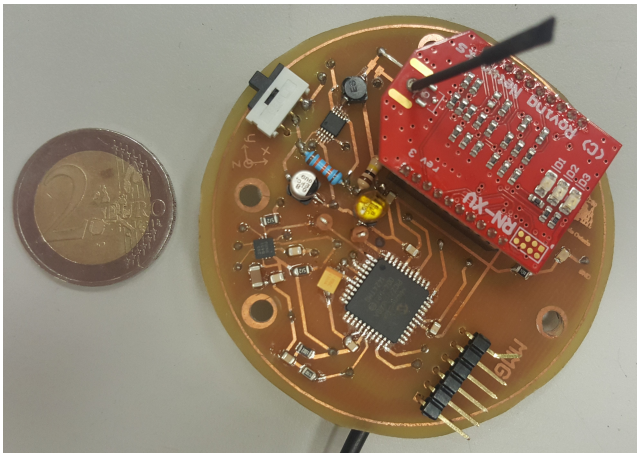

Figure 4-4: Rotor vibration measurement prototype.

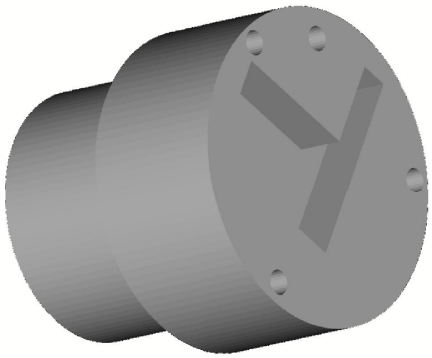

Figure 4-5: 3D printed plastic mounting.

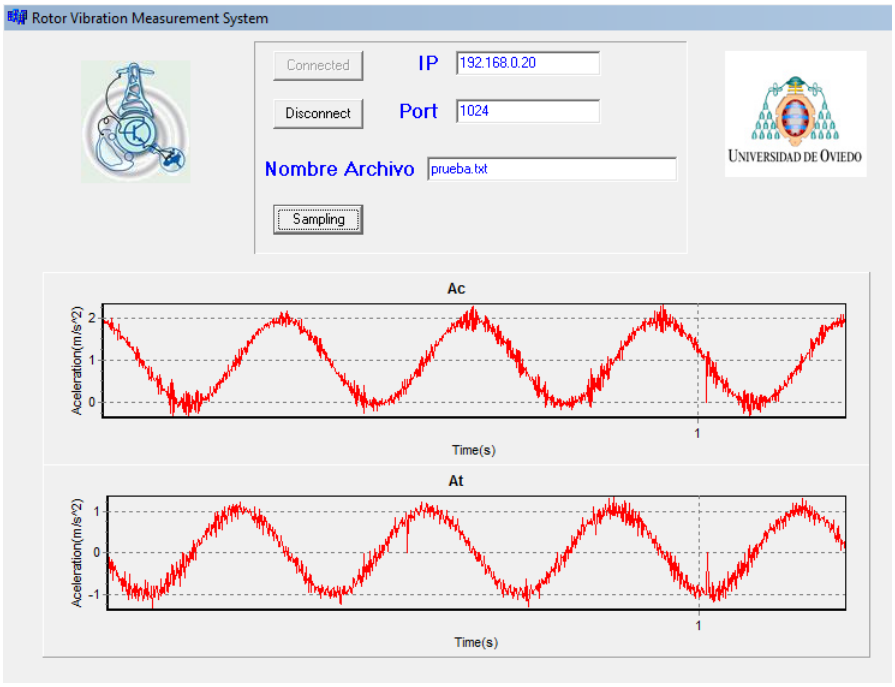

Figure 4-6: Window capture of the designed application to monitor rotor vibration.

Chapter 5

IPMSM Experimental Results

In the following chapter, the experimental setup used to test the prototype and the results for different tests are given. Since low speed ranges will cause large torque pulsation and, consequently large speed fluctuations, large harmonic distortion will appear on the frequency analysis of the measured acceleration signals. In order to get an accurate measurement system, an off-line digital signal processing have been conducted. This procedure has been validated through FEM simulations of the real machine.

5.1 Setup for rotor vibration tests

A set of tests have been conduced in order to validate both torque modelling of PMSMs and the performance of the rotor vibration measurement system. The designed prototype has been placed on the rotor shaft of a IPMSM driven by a 45kW, two poles induction machine. The power converter supplying both machines is a back-to-back converter in which the DC bus has been replaced by a DC/DC converter. The DC/DC converter allows to interchange the machine to be tested since the feeding voltage can be adapted to any machine requirement. The induction machine has been controlled with a closed loop speed control while, the PMSM is current controlled. A picture of the test bench used for rotor vibration measurement tests is shown in Fig.5-1.

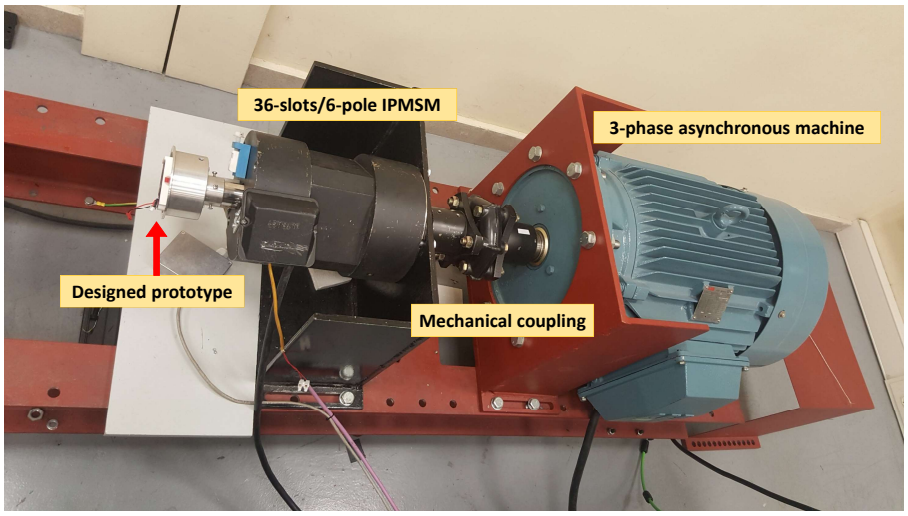

Figure 5-1: Experimental setup for rotor vibration measurement tests.

The first test that has been conducted is the measurement of the rotor tangential acceleration under no-load conditions. As stated in section 3.2.2, cogging torque will appear even when there is no current flow. Thus, according to (3.11), an acceleration harmonic should appear at a frequency equal to the LCM of the number of slots and poles of the PMSM, which in this case is 36. The test has been performed with a fixed speed of 20rad/s. Measurement of the tangential acceleration is shown in Fig.5-2.

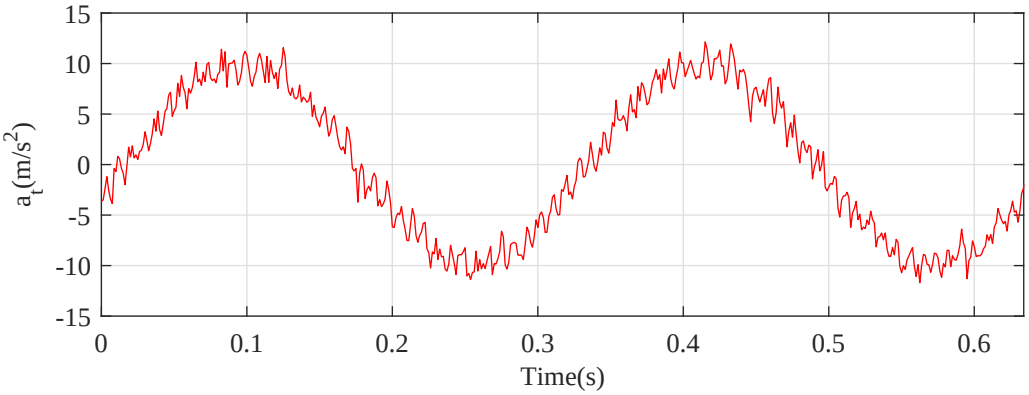

Figure 5-2: Experimental results: measurement of the tangential acceleration of the IPMSM shaft. i_{dq}=0 ω_m= 20rad/s.

It is observed from Fig. 5-2 that the tangential acceleration follows a sinusoidal profile. That's owing to the fact that Earth's gravity is measured by the accelerometer. Gravitational acceleration is a stationary variable always pointing perpendicular to the Earth's surface. However, since the axes of the accelerometer are rotating synchronously with the shaft, Earth's gravity is seen as a time-dependent variable with a frequency equal to the mechanical speed (see Fig. 5-3). This is a very a interesting feature since offers the possibility of estimating the mechanical speed/position of the rotor shaft.

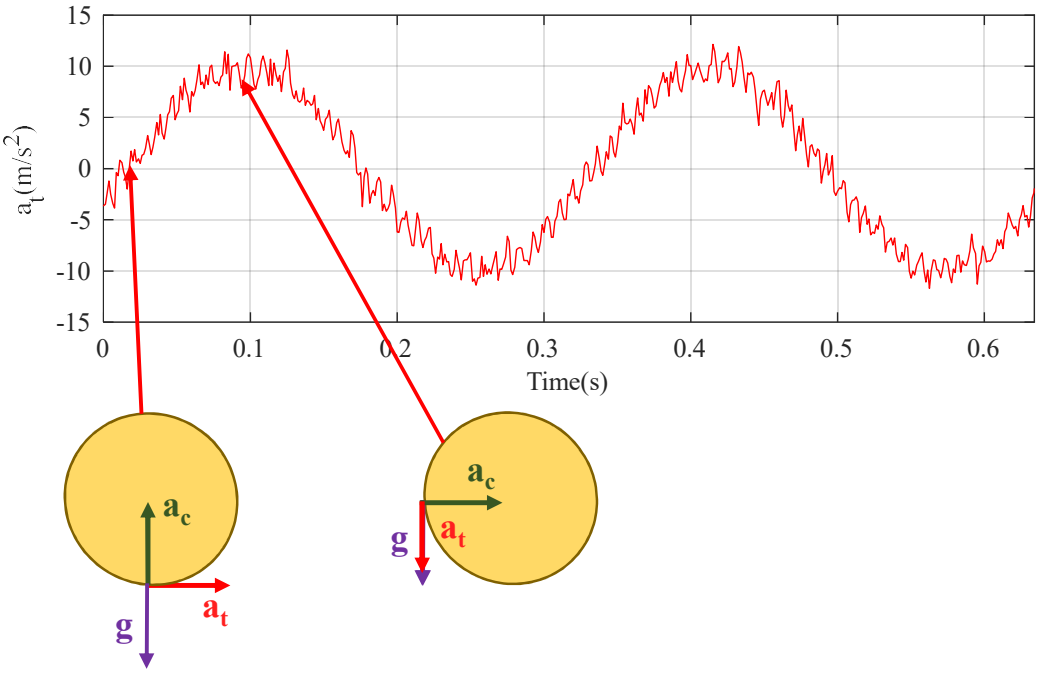

Figure 5-3: Effect of the Earth's gravity in the acceleration measurement. Yellow circles represent the PCB rotating synchronously with the rotor shaft.

Applying a FFT analysis to the acceleration time-waveform, its corresponding spectra is displayed in Fig. 5-4. Frequencies are normalized with respect to the mechanical fundamental frequency, 3.18Hz.

It is concluded from the FFT analysis that acceleration ripple appears at the thirty sixth harmonic of the mechanical frequency. This suggests that both mathematical model and designed prototype can be validated. However, even if the obtained results are highly satisfactory, Fig. 5-5 shows a zoom in the 36^{th} order harmonic to verify

the accuracy of the measurement system.

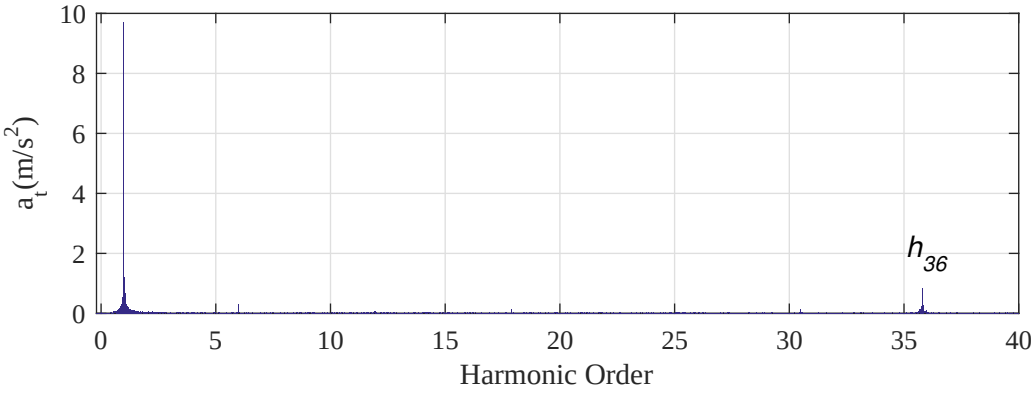

Figure 5-4: Experimental results: frequency spectrum of the tangential acceleration. i_{dq}=0 ω_m= 20rad/s.

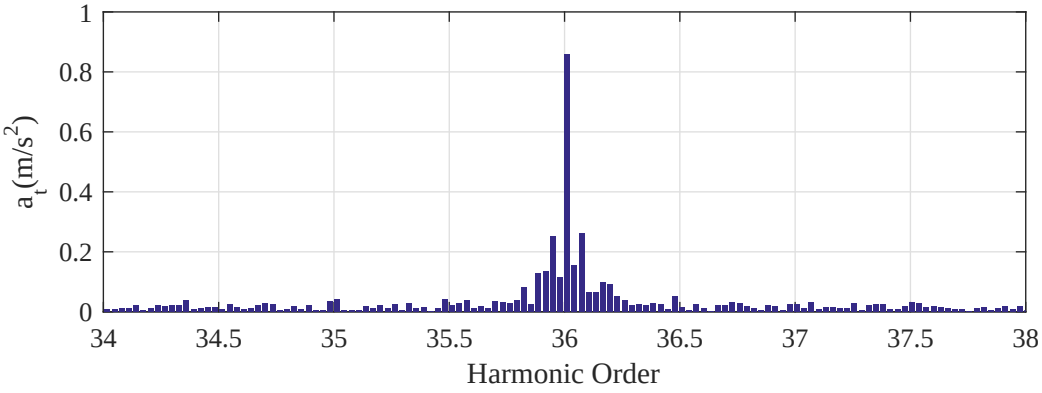

Figure 5-5: Zoom of the thirty sixth harmonic of the tangential acceleration.

The harmonic distortion observed in Fig. 5-5 is a shortcoming that makes losing accuracy on the machine characterization. There are several reasons to have harmonic distortion in the acceleration measurements.

- **Spectral Leakage**. It happens when the analyzed signal is not periodic in the interval (N samples). Signal frequency does not correspond exactly with the frequencies of the spectrum, so spectral components fall among several harmonics.

- **Errors on the speed control**. High-frequency torque ripple will reflect on the output shaft creating speed fluctuation. Bandwidth of the closed loop speed

control could not be fast enough to eliminate these high frequency speed fluctuations, distorting the acceleration spectra.

5.2 Digital signal processing

As stated before, measurement of the Earth's gravity offers the possibility to estimate the real speed of the machine. Since torque ripple appears at integer multiples of the fundamental speed, an improvement on the machine characterization could be achieved applying an off-line digital signal processing. This section covers the speed estimation and harmonic isolation procedure.

5.2.1 Rotor speed synchronization

Smooth and fast estimation of the mechanical speed of PMSMs is a key issue broadly investigated nowadays. There are several synchronization methods in order to estimate the speed of electrical machines eliminating the need of expensive position sensors. A brief summary outlining the main advantages and drawbacks of the most broadly used are explained below [18].

- **atan function** is likely the most intuitive solution. However, since atan function is a non-linear trigonometric discontinuous function it has significant shortcomings that makes it a poor selection for speed estimation. The main drawbacks are large computational requirements or the need of differentiation to obtain the rotor speed (problematic in practice due to noise).

- **Complex Phase Locked Loop (CPLL)**. This technique is based on the cross-product between a dq-complex vector and a unitary vector containing the estimated phase. In the stationary reference frame, phase error is obtained from the resulting vector product. The main advantage of this computational method is that do not involve discontinuous trigonometric calculations and both phase angle and frequency of the input signal are easily obtained. Fig. 5-6 shows the block diagram of the CPLL method.

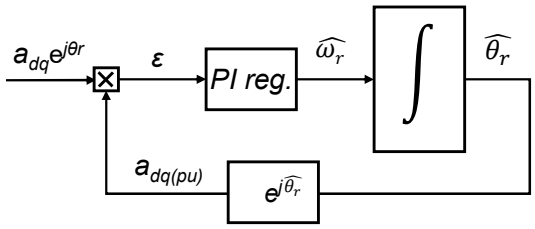

Figure 5-6: Block diagram of the complex phase locked loop (CPLL).

- **Synchronous reference frame (SRF-PLL)**. Complex PLL implemented in a synchronous reference frame leads to this simple computational method. Because it does not requires cross product, speed estimation involves less computational time so, this technique is broadly used in industrial applications.

The selected topology for rotor speed synchronization is the SRF-PLL because its simplicity of implementation, robustness and good dynamic response. Fig. 5-7 shows the block diagram of the SRF-PLL method.

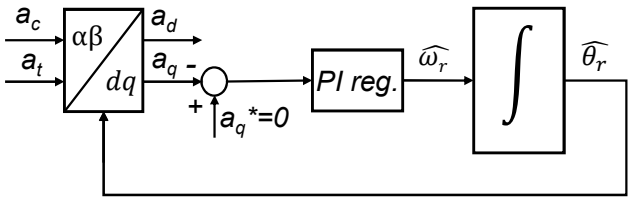

Figure 5-7: Block diagram of the synchronous reference frame phase locked loop (SRF-PLL).

Since gravity acceleration will be reflected on the xy-axes of the accelerometer, which are rotating synchronous with the rotor shaft, it will cause two sine waves 90 degrees out of phase. In other words, this behaviour is similar to a complex vector rotating in a stationary reference frame. Thus, applying the Park transformation to the acceleration complex vector, which is the quadrature of radial acceleration and tangential acceleration, the resulting complex vector can be expressed on a d-q rotor synchronous reference frame (5.1).

$$a_T^r = a_d + ja_q = (a_c + ja_t)e^{-j\omega_r t} \tag{5.1}$$

By forcing the q-axis component of the acceleration complex vector, a_q, to be zero by the closed control loop shown in Fig. 5-7, the d-axis component will be equal to the magnitude of the acceleration complex vector. The control effort signal of the PLL PI-controller will be the estimated speed of the rotating shaft. Any change of the mechanical speed rated value will give rise to errors in the PLL synchronization since d-axis will not be perfectly aligned with the acceleration complex vector. Finally, the rotor position can be easily obtained by integrating the estimated mechanical speed.

The main drawback of this method is that its performance can be compromised when the reference signal contains low-frequency harmonics. In order to not lose accuracy on the speed estimation, the PI controller has been tuned to have a bandwidth of 3Hz using the Matlab tool, sisotool. For such a small bandwidth, the PLL will not be able to follow high frequency harmonics but it will lose dynamic capability. Furthermore, a filtering stage has been designed to isolate the gravity acceleration from the overall acceleration vector. This filtering stage consists of rejecting low frequency harmonics by a combination of band-stop filters (BSF) and high-pass filters (HPF).

5.2.2 Filter Stage

As stated in section 3.2 and proven by the experimental results shown in Fig.5-2, when the machine is rotating under no-load conditions, cogging torque will appear at multiples of thirty six of the mechanical frequency. Moreover, when current is injected in the machine, torque ripple may also appear at multiples of six of the electrical frequency. Therefore for a six pole machine, acceleration ripple at the eighteenth harmonic will arise. Consequently, in order to improve the PLL performance, it is needed to separate the gravity acceleration from the overall acceleration complex vector. To do so, a filter stage will be needed as explained below.

- **High-pass filter (HPF)**. Equation (4.3) establishes that static torque can be monitored through the centripetal acceleration. Thus, the first step to isolate

gravitational acceleration is to eliminate the DC magnitude of the acceleration complex vector. Note that machine is rotating at very low speed rates. Thus, a trade off between filtering the magnitude of the DC component without affecting the gravitational acceleration has to be achieved. To do so, a second-order HPF with a bandwidth of 4Hz is applied to the acceleration complex vector (5.2).

$$G_{HPF}(s) = \frac{s^2}{s^2 + 2\omega_{bw}s + \omega_{bw}^2} \tag{5.2}$$

Where ω_{bw} is the bandwidth of the HPF in rad/s, defined as $2\pi f$. Fig. 5-8 shows the bode plot of the implemented HPF.

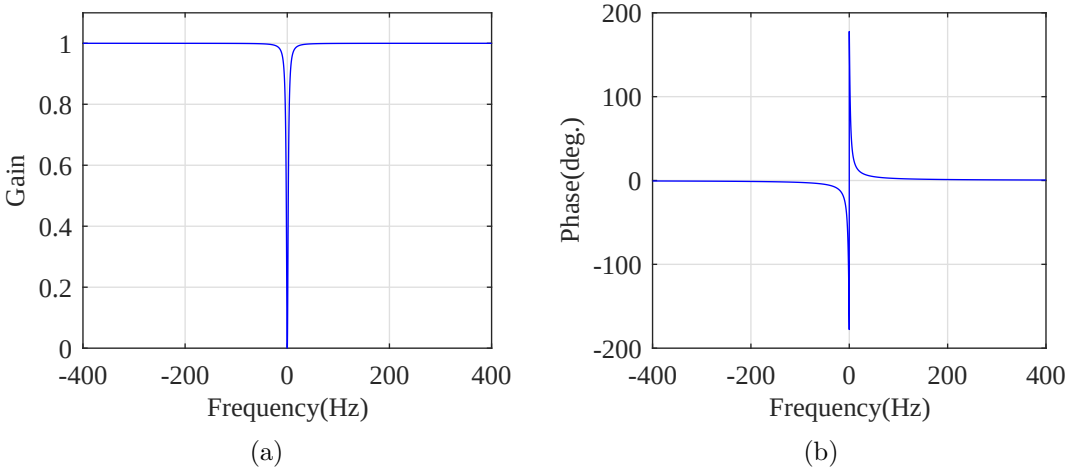

Figure 5-8: (a) Gain and (b) phase of the high pass filter.

- **Band-stop filter (BSF)**. In order to prevent the PLL reaction to high-frequency acceleration harmonics, second-order band-stop filters, also knows as band-rejection filters, have been implemented at multiples of ±18 and ±36 of the mechanical speed (5.3). Note that other harmonics band may also be filtered if their magnitude are large enough to compromise the performance of the PLL.

$$G_{BSF}(s) = \frac{s^2 + \omega_{hf}^2}{s^2 + \omega_{bw}s + \omega_{hf}^2} \tag{5.3}$$

Where ω_{hf} is the frequency of the harmonic to be eliminated and, ω_{bw} the bandwidth of the BSF. Fig.5-9 shows the bode plot of the implemented BSF

for the rejection of the 18^{th} acceleration harmonic.

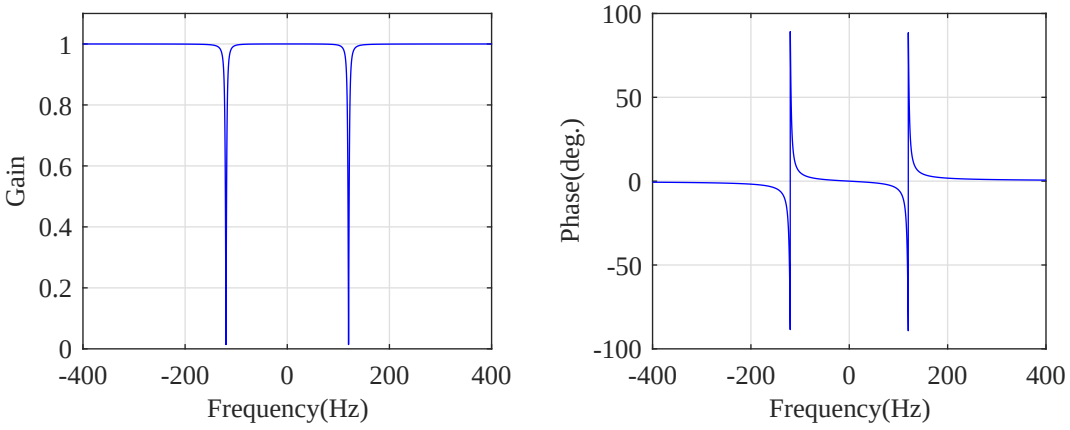

(a) (b)

Figure 5-9: (a) Gain and (b) phase of the band stop filter at ω_{hf}.

- **Low-pass filter (LPF)** Finally, acceleration complex vector is rotated to positive sequence synchronous reference frame. In this reference frame, the gravity acceleration will be a DC magnitude. Thus, applying a second-order LPF, gravity acceleration can be perfectly isolated. The transfer function of a second-order LPF is given by (5.4).

$$G_{LPF}(s) = \frac{\omega_{bw}^2}{s^2 + 2\omega_{bw}s + \omega_{bw}^2} \tag{5.4}$$

  Fig.5-10 shows the bode plot of the implemented LPF, with a bandwidth of 2Hz.

With the gravitational acceleration isolated from the overall acceleration complex vector, rotor speed synchronization can be performed.

Once the speed estimation is obtained, a second filtering stage has to be conduced to isolate high-frequency acceleration harmonics from the overall complex vector. As an example, the needed steps to extract the 36^{th} harmonic component are as follows (see Fig. 5-11).

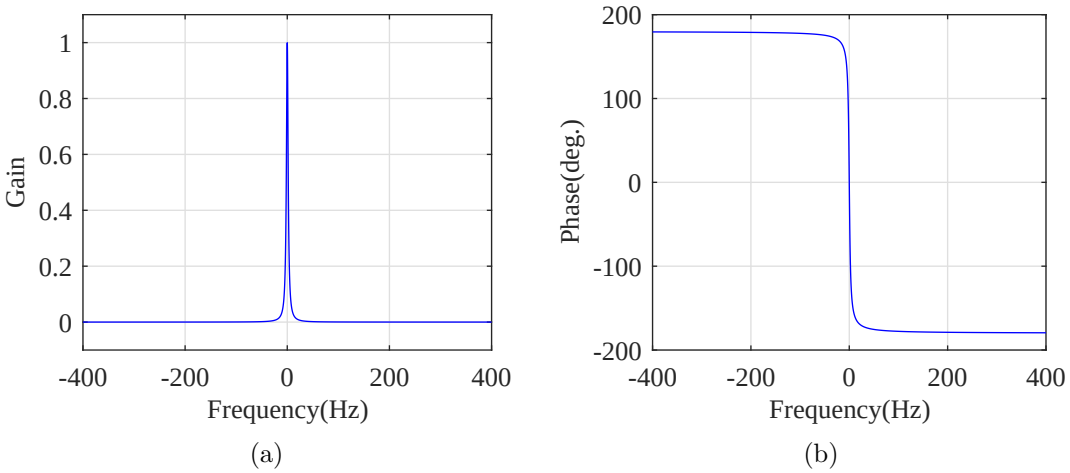

Figure 5-10: (a) Gain and (b) phase of the low pass filter.

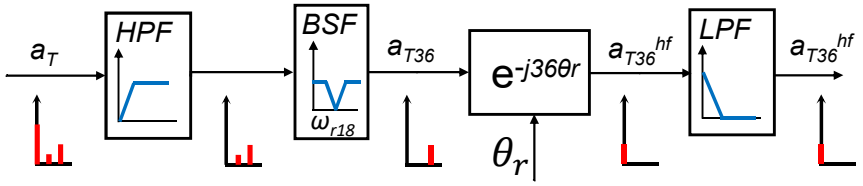

Figure 5-11: Block diagram for harmonic isolation.

- High-pass filtering to remove the DC component of the acceleration complex vector.

- Band-rejection filtering at ω_r and ω_{hf} to remove the gravitational acceleration component and relevant harmonic bands.

- Transformation to harmonic synchronous reference frame (5.5). In this reference frame, the 36^{th} acceleration harmonic will be a DC magnitude.

$$a^{hf} = (a_c + ja_t)e^{-j\omega_{hf}t} \tag{5.5}$$

- Low-pass filtering to isolate the 36^{th} acceleration harmonic. By averaging the isolated harmonic component, increased preciseness in machine characterization can be achieved.

5.2.3 Validation

Before implementing the digital signal processing to the experimental results, it is advantageous to validate both the rotor speed synchronization method and filtering stage in a FEM simulation. By means of a previously developed FE model of the real machine, where only some parameters of the machine such as the rotating speed or feeding currents were needed to be changed, a batch of tests have been performed for a number of feeding dq-currents ranging from -14A (1pu) to 14A(1pu).

As it was stated in section 3.2, when dq-currents are injected to the machine, torque ripple may appear at the rotor shaft. In addition, negative d-axis current may be also injected to vary the PM flux, in a process known as flux weakening. As a consequence, magnitude of cogging torque and torque ripple will vary according to the current injection.

A first simulation has been conduced with the FE machine model working under no-load conditions and a fixed mechanical speed of 62rad/s. Rotor speed estimation has been implemented using the stator voltages from the simulation results. Fig. 5-12 shows the results of the validation of the rotor speed synchronization method.

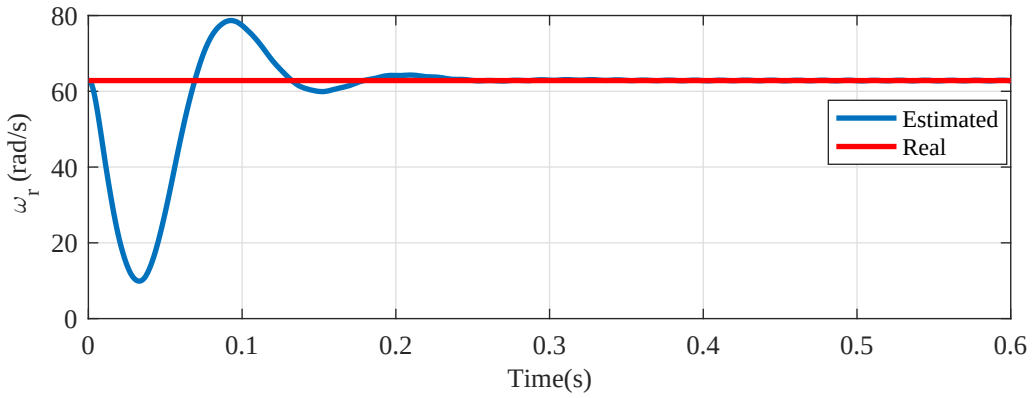

Figure 5-12: Validation of the digital signal processing: Real speed vs estimated speed. $i_{dq} = 0$ and $\omega_r = 62$ rad/s.

From the results shown in Fig 5-12, it can be observed the good dynamic response of the rotor synchronization method. The estimated speed is approximately equal to the mechanical speed of the FEM simulation and it follows the reference with a low settling time. Thus, the rotor speed synchronization method can be validated.

Fig. 5-13 shows the torque harmonic variation as a function of the injected current. Torque harmonics from the FFT analysis given by the FEM simulations have been compared with the magnitude extracted from the filtering stage.

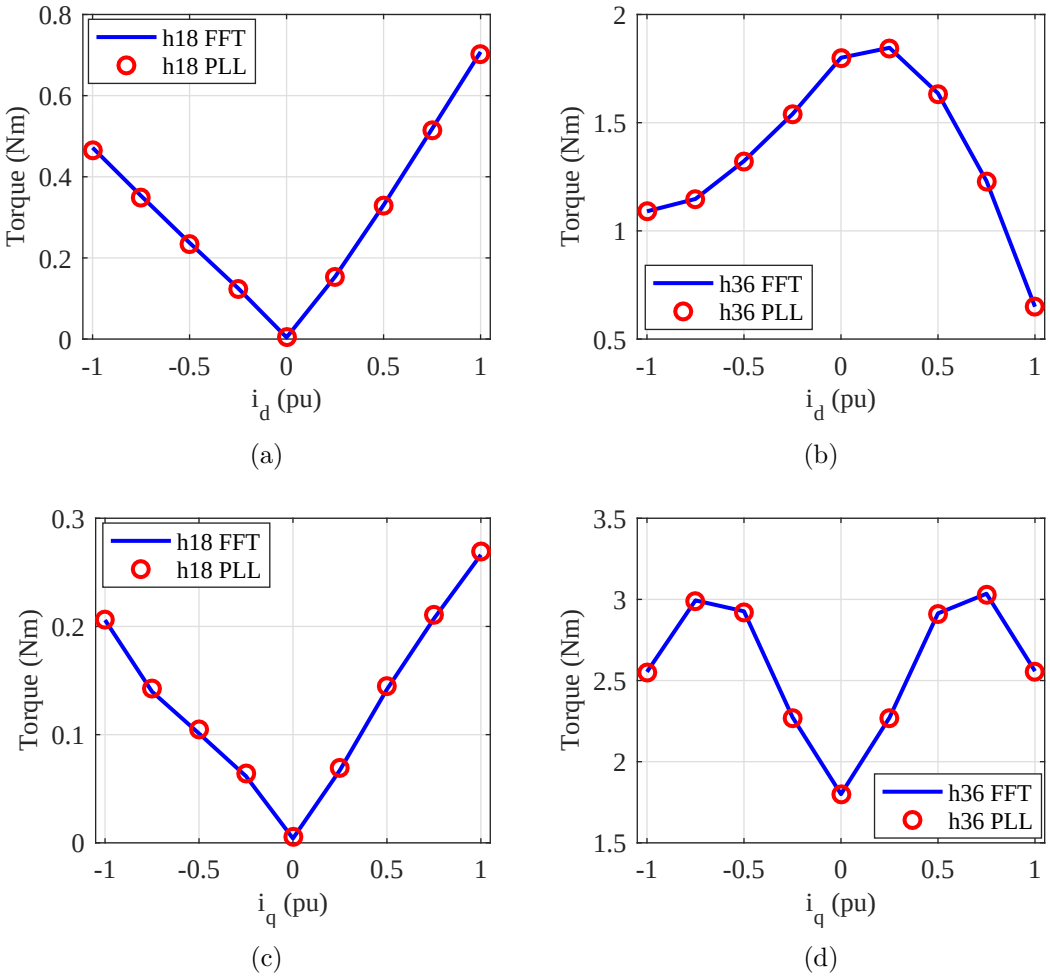

Figure 5-13: Validation of the digital signal processing: Torque pulsation as a function of the injected current. (a) 18^{th} torque harmonic vs i_d (b) 36^{th} torque harmonic vs i_d (c) 18^{th} torque harmonic vs i_q (d) 36^{th} torque harmonic vs i_q.

Note that the scale of the graphics are not all equal in order to proper see the harmonic dependence with the injected current. From the simulation results shown in Fig. 5-13, it is observed the equivalence between the harmonics given by the FEM simulations and those extracted from the filtering stage. It can be concluded that the filtering stage results are highly satisfactory, validating the digital signal processing.

5.3 Experimental results

Once the digital signal processing has been validated, measurement of the shaft vibration have to be also processed to verify the accuracy of the rotor vibration measurement system. The same tests as for the FEM simulations have been conduced for the IPMSM. These tests have been conduced for the real machine rotating at 20rad/s. Fig. 5-14 shows the mechanical speed estimation obtained from the SRF-PLL.

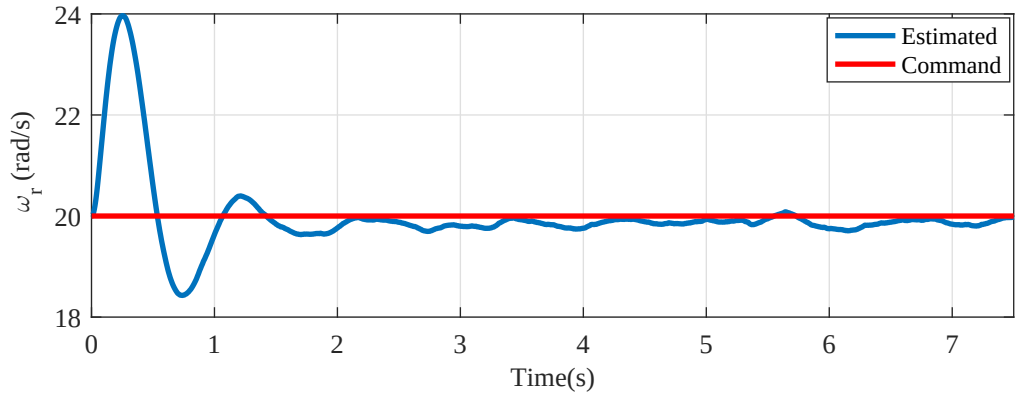

Figure 5-14: Mechanical speed estimation from measured acceleration data.

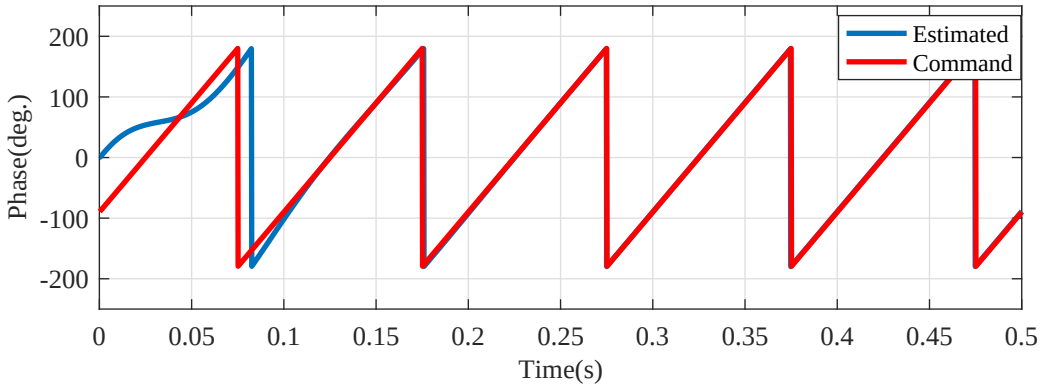

Figure 5-15: Rotor position estimation from measured acceleration data.

It can be observed from the experimental results shown in Fig. 5-14, that, as it was expected, torque pulsation causes large speed fluctuations on the rotor shaft.

By integrating the speed, the rotor position can also be obtained as shows Fig.5-15. Thus, tangential acceleration can be given as a function of the mechanical position. Fig. 5-16 shows a comparison between the measured tangential acceleration and the simulated torque waveform from FEM simulations. Both signals have been obtained with the machine working under no-load conditions. Note that the gravity acceleration has been filtered from the tangential acceleration shown in Fig. 5-2 in order to proper compare both signals. This filtering stage has been implemented using a BSF as it has been previously explained.

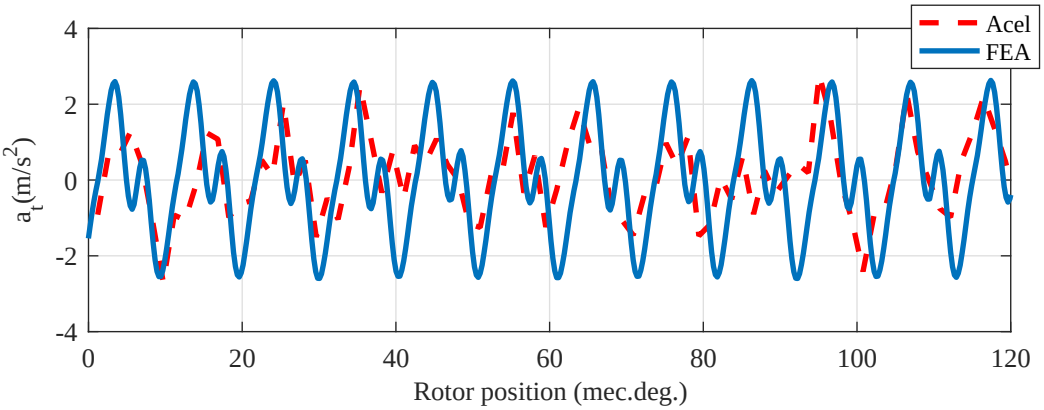

Figure 5-16: Validation of the rotor vibration measurement system: Comparison between measured acceleration and simulated torque.

It is observed from the comparison shown in Fig. 5-16 that both measured data and experimental results follow the same tendency, with a period of 10 mechanical degrees. Thus, both waveforms fulfill the mathematical model given in (3.11). Therefore, it can be confirmed that cogging torque estimation of a real machine is measured from the designed prototype.

Finally, to conclude the experimental validation, tangential acceleration harmonics tendency as a function of the injected current are shown in Fig. 5-17 and Fig. 5-18. Note that only harmonic tendency can be compared since the inertia coefficient of the electrical machine has not been estimated so far. However, the expected behaviour is that the measured acceleration harmonics follow a similar behaviour as the torque harmonics of the FEM simulations.

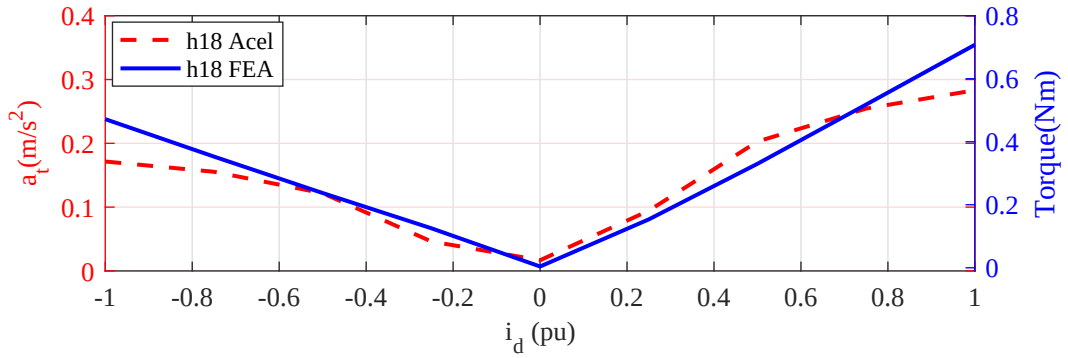

(a)

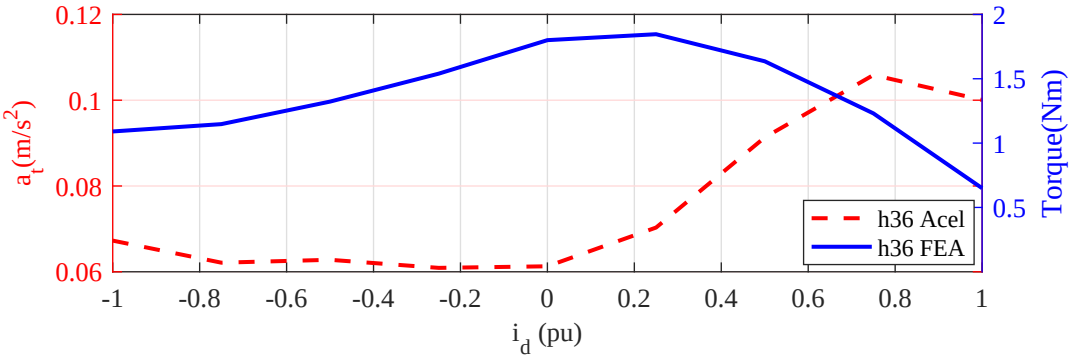

(b)

Figure 5-17: Validation of the rotor vibration measurement system: Comparison between acceleration and torque pulsation as a function of the injected current. (a) 18^{th} harmonic vs i_d (b) 36^{th} harmonic vs i_d.

It is concluded from the experimental results shown in Fig. 5-17 and Fig.5-18 that approximately the same tendencies are observed both for the acceleration and torque harmonics. Thus, the designed prototype can be validated. Differences between simulation and experimental results may be due to a number of factors, such as different characteristics of the PMs, iron or copper materials, assembly tolerances, etc.

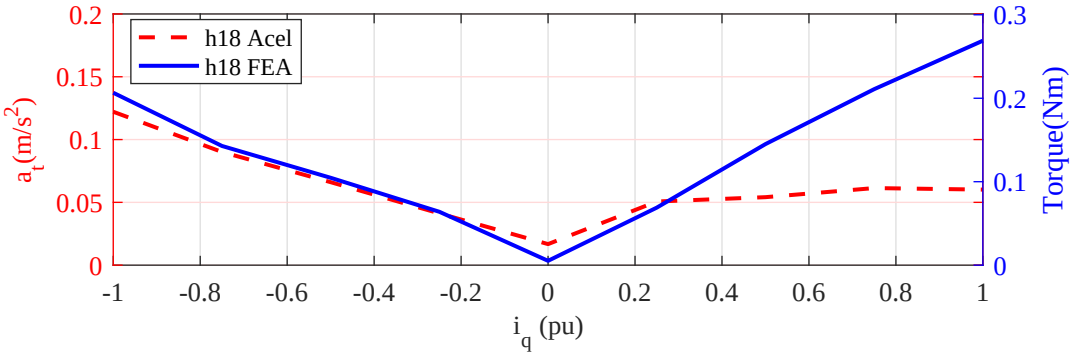

(a)

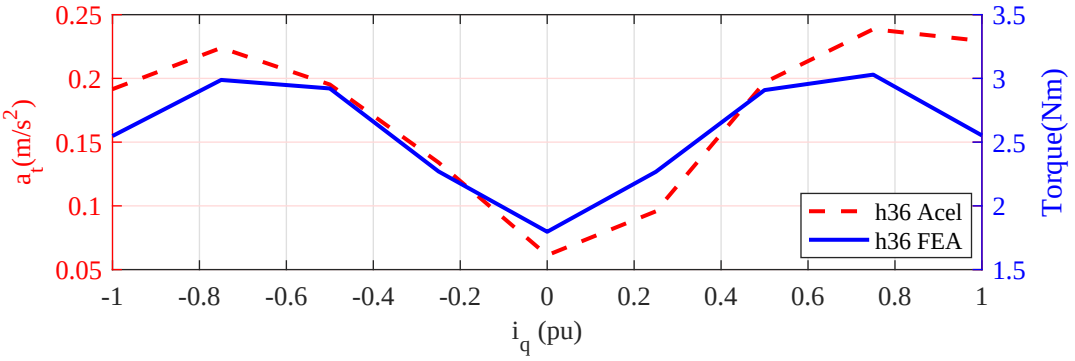

(b)

Figure 5-18: Validation of the rotor vibration measurement system: Comparison between acceleration and torque pulsation as a function of the injected current. (a) 18^{th} harmonic vs i_q (b) 36^{th} harmonic vs i_q.

Chapter 6

Torque Harmonic Compensation

This Master Thesis has been focused on the development of a rotor vibration measurement system to monitor torque pulsation at the rotating shaft of a IPMSM. The designed prototype has been validated on the previous chapter by comparing the experimental results with FEM simulations. As it has been stated, the designed prototype may be useful for machine characterization but it can also be used for harmonic compensation. In the following chapter, the development of a control strategy for harmonic compensation is given. The aim of the proposed model is to integrate the measurement of the torque harmonics in the control strategy of the machine in order to compensate high-frequency torque pulsation.

6.1 Proposed control strategy for torque harmonic compensation

In order to implement a control strategy for torque harmonic compensation, the IPM machine model has to be implemented in a transient simulation, using the simulation software Simulink®. Fig. 6-1 shows the control block diagram for the harmonic compensation. Once the dynamic electrical model of the machine is implemented in the simulation software, PI regulators are used to control the injected current. To design a control strategy as close to reality as possible, it is assumed that only output

torque can be measured. A filtering stage is used to isolate the torque harmonics to be compensated. Finally, high-frequency harmonics will be neutralised with a resonant control.

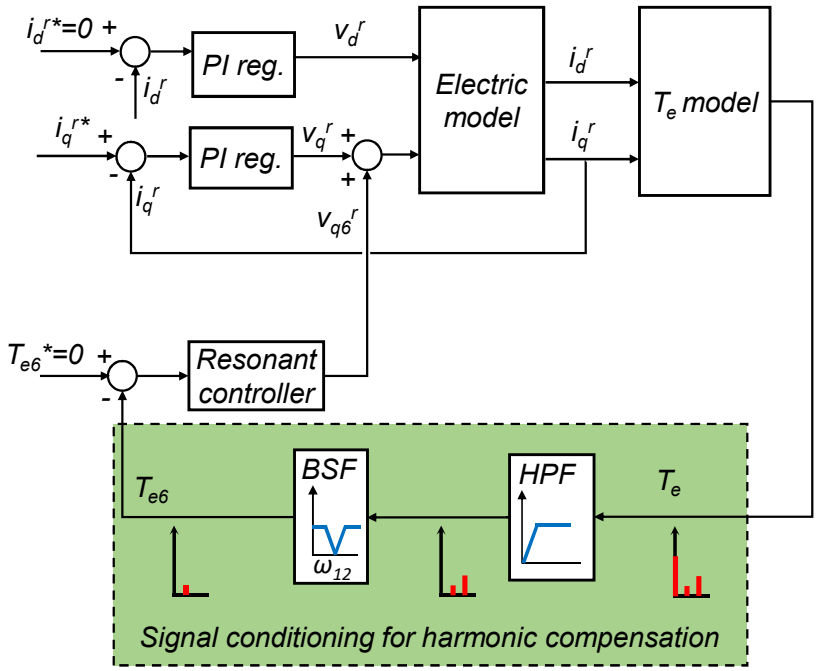

Figure 6-1: Block diagram of the proposed torque harmonic compensation control.

6.1.1 Dynamic model of the IPMSM with saliency

In order to perform the transient simulation of the motor, the electrical model given in section 3.1.1 has to be implemented in the simulation software, Simulink®. It has to be noted, however, that the electrical model does not model the machine saliencies. In other words, neither the winding inductances or the PM flux linkage are modelled with spatial dependence. Thus, an inductance variation with the rotor position has to be included in the electrical model of the IPMSM (6.1). The PM flux linkage is also spatial dependent as stated in section 3.2, so it can be modelled as (6.2) [19].

$$\begin{bmatrix} L_{ds}(\theta_r) & 0 \\ 0 & L_{qs}(\theta_r) \end{bmatrix} = \begin{bmatrix} L_{d0} + \Delta_{(pu)} L_{d0} sin(h(\theta_r + \phi_r)) & 0 \\ 0 & L_{q0} + \Delta_{(pu)} L_{q0} cos(h(\theta_r + \phi_r)) \end{bmatrix} \tag{6.1}$$

$$\lambda_{PM}(\theta_r) = \lambda_{PM0} + \Delta_{(pu)} \lambda_{PM0} sin(h(\theta_r + \phi_r)) \tag{6.2}$$

The subscript 0 represents the DC magnitude of both inductances values and PM flux linkage. The inductance variation could be approximately modelled including a small variation with respect to the DC magnitudes. However, in order to develop a more realistic simulation model, three FEM simulations have been conduced to extract the inductances and flux linkage variation with rotor position.

- A first simulation has been carried out with the FE machine model working under no-load conditions ($i_d^r = 0$; $i_q^r = 0$). From (3.1) and (3.2), the dq-stator voltages in the rotor reference frame with i_{dq}^r set to zero are given by (6.3) and (6.4).

$$v_d^r = 0 \tag{6.3}$$

$$v_q^r = \lambda_{PM} \omega_r \tag{6.4}$$

  Isolating λ_{PM} in (6.4), the PM flux linkage can be defined as:

$$\lambda_{PM} = \frac{v_q^r}{\omega_r} \tag{6.5}$$

  Thus, the PM flux linkage can be obtained by applying the Park transformation to the stator voltages given by the FEM simulation. Fig. 6-2 shows the PM flux linkage variation with rotor position and the corresponding frequency spectra. Note that frequencies are normalized with respect to the electrical fundamental frequency, 10Hz. Thus, at was expected, PM flux linkage harmonics appear at multiples of twelve of the electrical frequency.

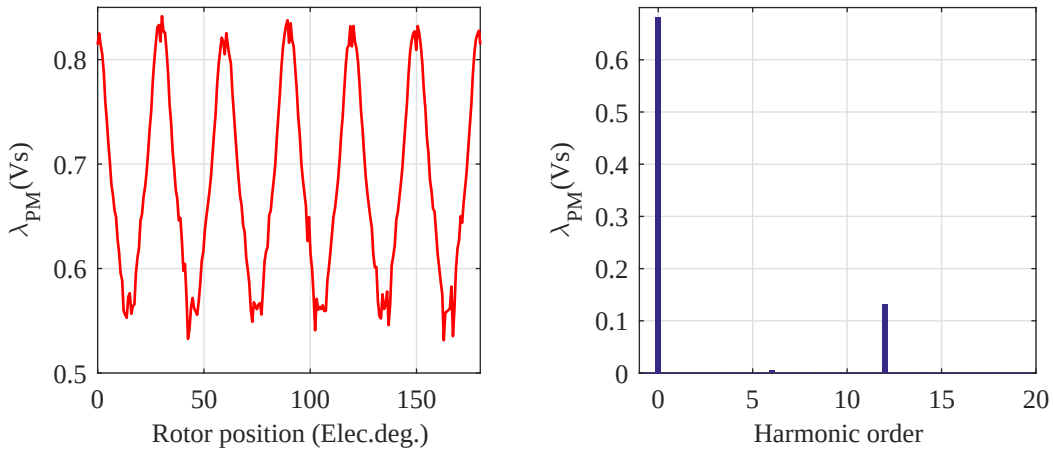

Figure 6-2: (a) PM flux linkage variation with rotor position (λ_{PM}) and (b) corresponding frequency spectrum i_{dq}=0.

- Following the same procedure, a second simulation has been carried out injecting 14A q-axis current in the FE machine model. From (3.1) and (3.2), the resultant dq-stator voltages with i_d^r set to zero are shown in (6.6) and (6.7).

$$v_d^r = -\omega_r L_{qs} i_q^r \tag{6.6}$$

$$v_q^r = R_s i_q^r + p L_{qs} i_q^r + \omega_r \lambda_{PM} \tag{6.7}$$

Neglecting transients and isolating the q-axis inductance from (6.6), it yields:

$$L_{qs} = \frac{-v_d^r}{\omega_r i_q^r} \tag{6.8}$$

Fig. 6-3 shows the q-axis inductance variation with rotor position and the corresponding frequency spectra. Note that, since the machine is current fed, q-axis inductance harmonics appear at multiples of six and twelve of the fundamental electrical frequency.

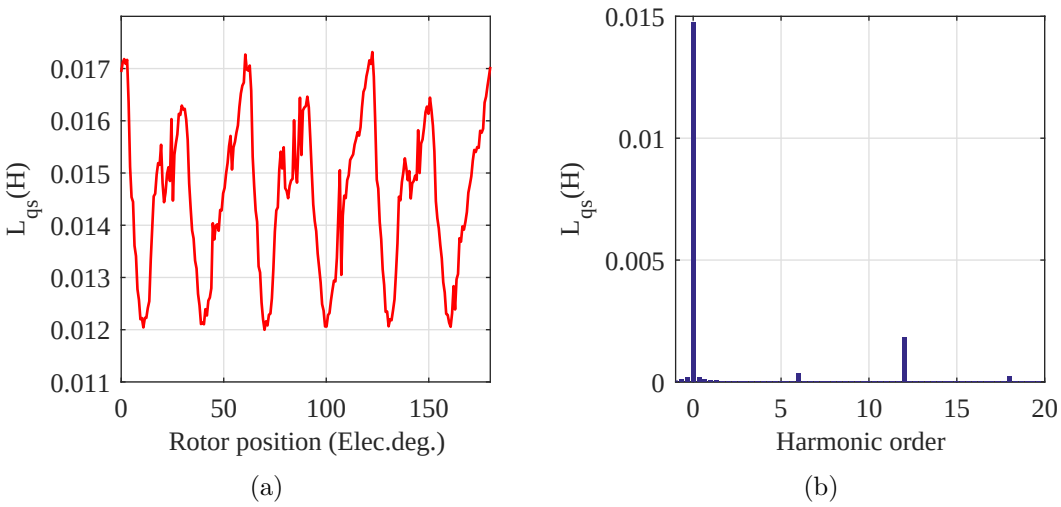

Figure 6-3: (a)q-axis inductance variation with rotor position (L_{qs}) and (b) corresponding frequency spectrum. $i_d^r = 0$, $i_q^r = 1pu$.

- Finally, a third simulation has been carried out injecting 14A d-axis current in the FE machine model. From (3.1) and (3.2), the dq-stator voltages with i_q^r set to zero are shown in (6.9) and (6.10).

$$v_d^r = R_s i_d^r + pL_{ds} i_d^r \tag{6.9}$$

$$v_q^r = \omega_r L_{ds} i_d^r + \omega_r \lambda_{PM} \tag{6.10}$$

  Note that the PM flux linkage given in (6.5) is needed to compute the d-axis inductance value (6.11). Fig. 6-4 shows the d-axis inductance variation with rotor position as well as the corresponding frequency spectra.

$$L_{ds} = \frac{v_q^r - \omega_r \lambda_{PM}}{\omega_r i_d^r} \tag{6.11}$$

With the machine parameters shown in Table 4.1 and the dq-inductance and PM flux linkage values as a function of the rotor position, the machine model can be now implemented in Simulink.

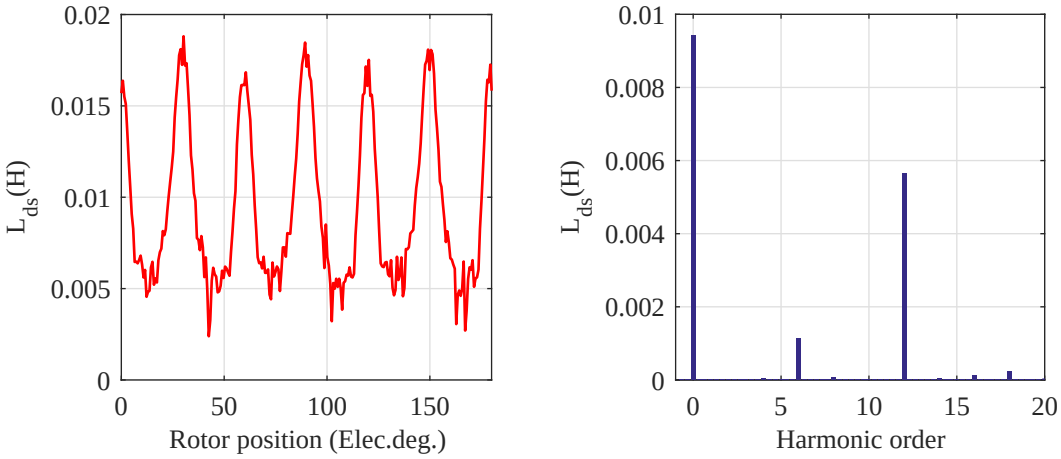

Figure 6-4: (a)d-axis inductance variation with rotor position (L_{ds}) and (b) corresponding frequency spectrum. $i_d^r = 1pu$, $i_q^r = 0$.

6.1.2 Current control

Aligning the current complex vector with the q-axis of the dq-rotor synchronous reference frame, current magnitude injected in the machine can be easily controlled. In order to do so, an armature current control loop has to be designed as shows Fig. 6-5.

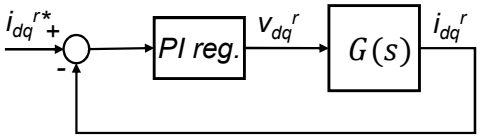

Figure 6-5: Block diagram of the closed-loop current control.

The electrical subsystem is only considered for simplification (6.12).

$$G(s) = \frac{1}{Ls + R_s} \tag{6.12}$$

It can be observed from (6.12) that the system to be controlled is a first order system with a pole placed at -R/L in open loop (type 0). Thus, the suitable controller to eliminate position errors and reject disturbances at steady state is a PI controller.The

transfer function of a PI controller is shown in (6.13).

$$PI_{reg}(s) = K_p + \frac{K_i}{s} = K_p \frac{s + \frac{K_i}{K_p}}{s} \tag{6.13}$$

Where K_p is the proportional gain and K_i the integral controller gain. From (6.13), it can be observed that the PI controller has a zero and a pole at the origin. In order to tune the PI controller, the zero-pole cancellation technique is applied. Therefore, the zero is placed on top the dominant pole of the open loop transfer function (6.14) and, the closed loop pole is freely moved for achieving the desired bandwidth(6.15).

$$\frac{K_i}{K_p} = \frac{R_s}{L} \tag{6.14}$$

$$K_p = 2\pi bw_c L \tag{6.15}$$

Where bw_c is the bandwidth of the closed current control loop in Hz . Note that two current controllers have to be tuned, according to the dq-inductance values L_{dq0} given in the previous section. Both controllers have been tuned with a bandwidth of 200Hz.

With the electrical model and the closed-loop current control implemented in the simulation software, Simulink®, the electromagnetic torque is obtained. Fig. 6-6 shows the resulting torque as well as the corresponding frequency spectra for the case of a q-axis current of 20A and a rotating speed of 20rad/s.

It is observed from the FFT analysis of the electromagnetic torque shown in Fig. 6-6(b) that both the static torque and torque ripple have been correctly modelled. Note that electromagnetic torque is an electrical variable, thus torque ripple appears at multiples of six of the fundamental electrical frequency. Also note that a detailed model of the machine, including different effects that can affect to the dynamics of the machine such as eccentricities or saturation effects, is a subject of ongoing research. However, the simulation results are highly satisfactory and can be validated in order to implement the proposed torque harmonic compensation control.

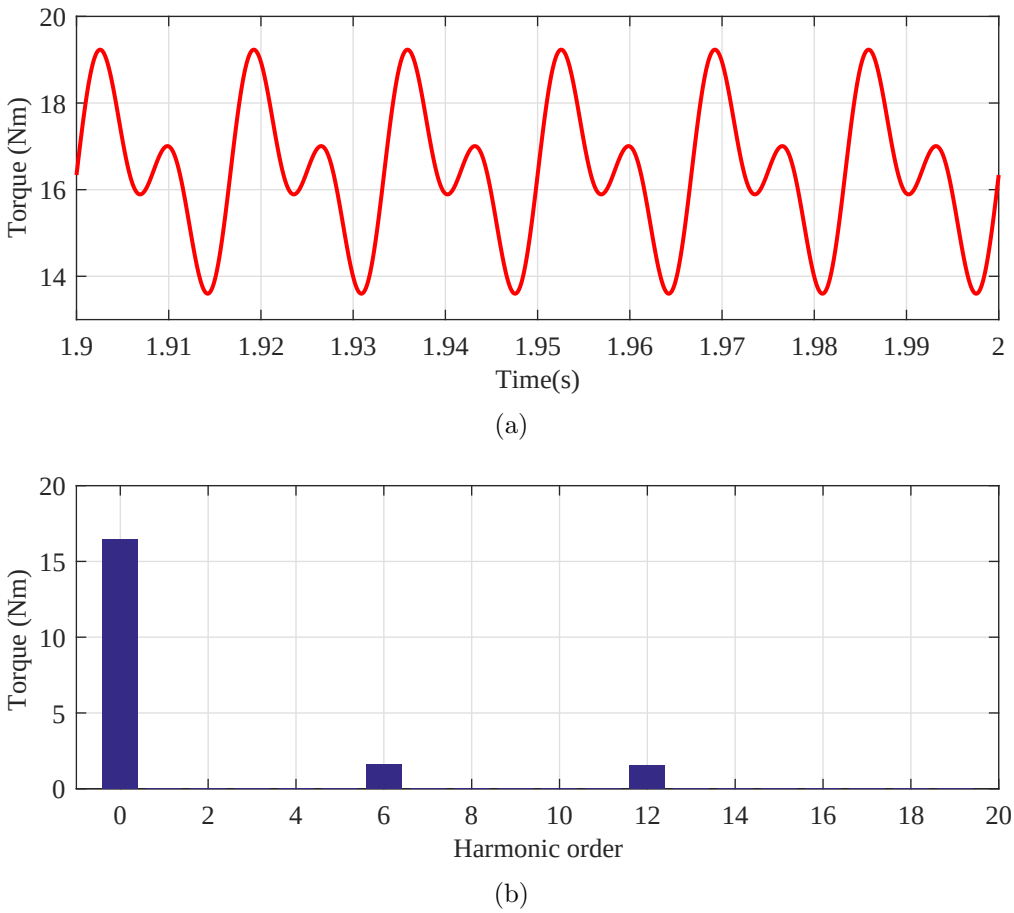

Figure 6-6: Results of torque harmonic compensation simulation: (a) Electromagnetic torque and (b) corresponding frequency spectrum. $iq^* = 20A$ and $f_e = 10Hz$ (b)

6.1.3 PR-Controller Design

The main advantage of PR-controllers is the capability of tracking sinusoidal signals with zero steady-state error. On the contrary of PI regulators, PR controllers have infinite gain at the AC fundamental frequency of the system, ω. However, one of the main drawbacks of PR controllers is the high reduction of the controller gain at frequencies different from the resonant freuqnecy. Therefore, the output signal is not able to track the reference sinusoidal signal with zero steady-state error [20].

The ideal resonant controller can be derived applying Euler's expression to a sinusoidal input signal:

$$sin(\omega \cdot t) = \frac{1}{2}\left(e^{j\omega} - je^{-j\omega}\right) \tag{6.16}$$

From Euler's formula it can be seen that a sinusoidal signal can be represented by two rotating vectors in opposite direction. Thus, two PI controllers have to be designed both for positive and negative frequencies:

$$PI_{(s=j\omega)} = K_p \frac{s - j\omega + \frac{1}{T_i}}{s - j\omega} \tag{6.17}$$

$$PI_{(s=-j\omega)} = K_p \frac{s + j\omega + \frac{1}{T_i}}{s + j\omega} \tag{6.18}$$

By adding (6.17) and (6.18), it yields:

$$PR(s) = 2K_p \cdot \frac{s^2 + \omega^2 + s\frac{1}{T_i}}{s^2 + \omega^2} \tag{6.19}$$

Where T_i is the time constant, K_p is the proportional gain of the resonant controller and, ω is the frequency of the harmonic to be compensated, ω_{hf}. The PR resonant controller have been tuned following the same procedure as for the current PI controller. Thus, following the zero-pole cancellation technique, the time constant and proportional gain of the resonant controller can be defined as:

$$K_p = 2 \cdot \pi \cdot bw_{PR} \cdot L_{qh} \tag{6.20}$$

$$T_i = \frac{L_{qh}}{R_s} \tag{6.21}$$

Where L_{qh} is the inductance harmonic value given in Fig. 6-3 and, bw_{PR} is the required bandwidth for the resonant converter in Hz. Note that a resonant controller has to be tuned for each torque harmonic. For the simulation, each resonant converter has been tuned with a bandwidth of 50Hz.

6.1.4 Signal filtering stage

To not disturb the PR-controller performance, the reference signal should only contain the frequency of the harmonic to be compensated, ω_{hf}. For that reason, a filtering stage to separate the torque harmonics from the overall torque signal will be needed

as explained in section 5.2.2. The methodology for the filtering stage is as shows Fig.6-1.

Firstly, a high-pass filter is applied to remove the DC component of the electromagnetic torque. Fig. 6-7 shows the resulting torque without the DC component. Then, a band-stop filter (BSF) is used to prevent the resonant converter reaction to other high-frequency signals. Fig. 6-8 and 6-9 shows the 6^{th} and 12^{th} torque harmonic components isolated from the overall torque signal.

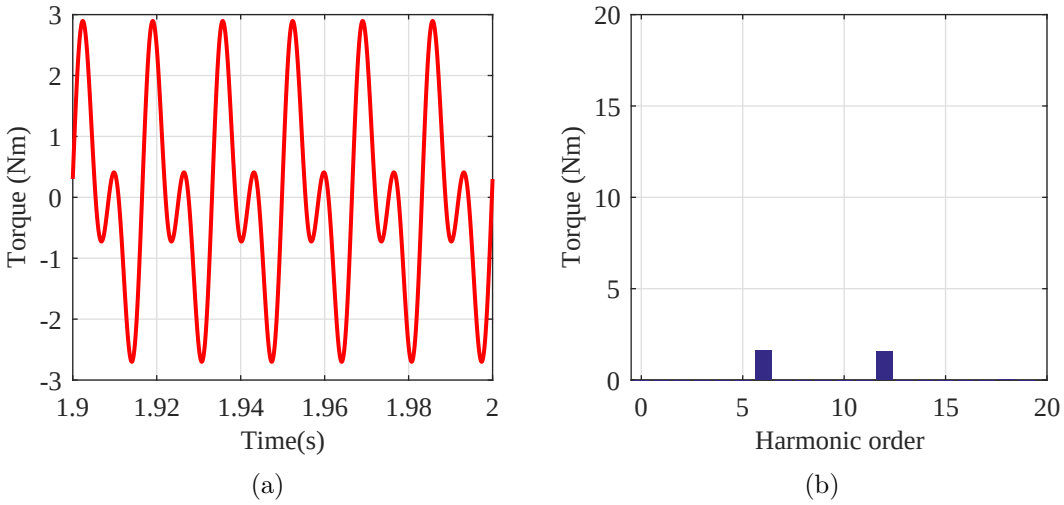

(a) (b)

Figure 6-7: Results of torque harmonic compensation simulation: (a) Electromagnetic torque without DC component and (b) corresponding frequency spectrum. $iq^* = 20A$ and $f_e = 10Hz$ (b)

Finally, the closed-loop control to reject such harmonics has been implemented in Simulink ®. Fig 6-1 shows the block diagram for the rejection of high-frequency torque pulsation. Note that Fig 6-1 shows the closed-loop control to compensate the 6^{th} torque harmonic. Same procedure is followed for the 12^{th} torque harmonic compensation. The high-frequency signals from the output of the PR-controller will be added on top of the PI controller output voltage.

Fig. 6-10 shows a comparison between the electromagnetic torque without high-frequency torque compensation and the electromagnetic torque once the proposed control strategy has been applied. It can be observed from the simulation results that torque ripple is highly diminished. Although higher order components have not

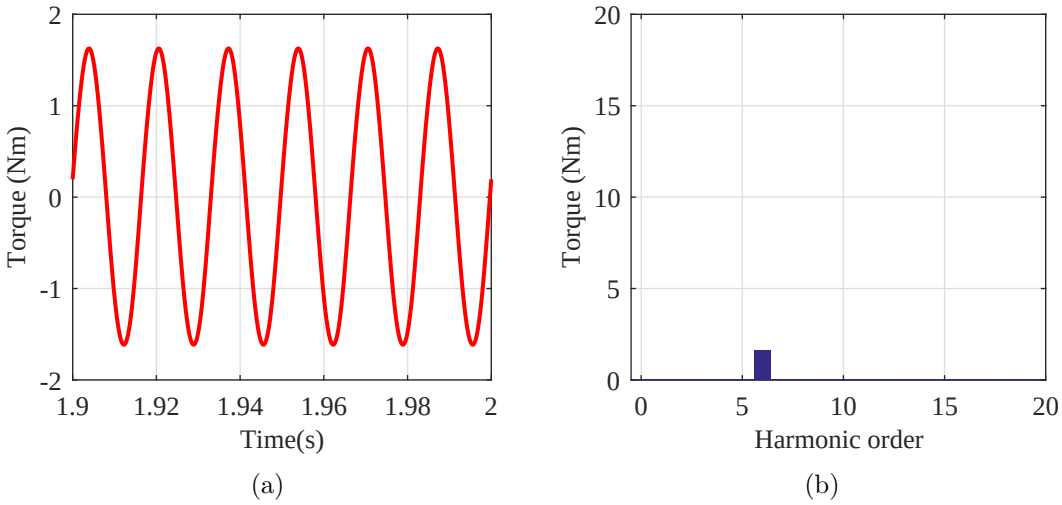

Figure 6-8: Results of torque harmonic compensation simulation: (a) Electromagnetic torque without the 12^{th} harmonic component and (b) corresponding frequency spectrum. $iq^* = 20A$ and $f_e = 10Hz$ (b)

been compensated, they can be neglected since the torque ripple profile is lower than 3%. Thus, it is concluded that the proposed control strategy is working properly.

Therefore, in future designs, measurement of the rotor vibrations may be implemented in the control strategy of the machine to compensate torque pulsation. This is a very interesting feature for improving the smooth torque production of PMSMs.

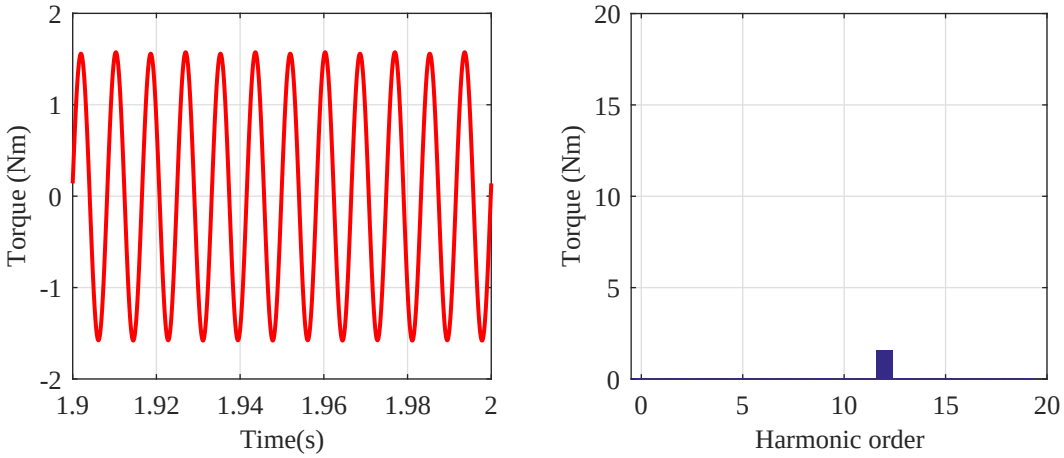

Figure 6-9: Results of torque harmonic compensation simulation: (a) Electromagnetic torque without the 6^{th} harmonic component and (b) corresponding frequency spectrum. $iq^* = 20A$ and $f_e = 10Hz$ (b)

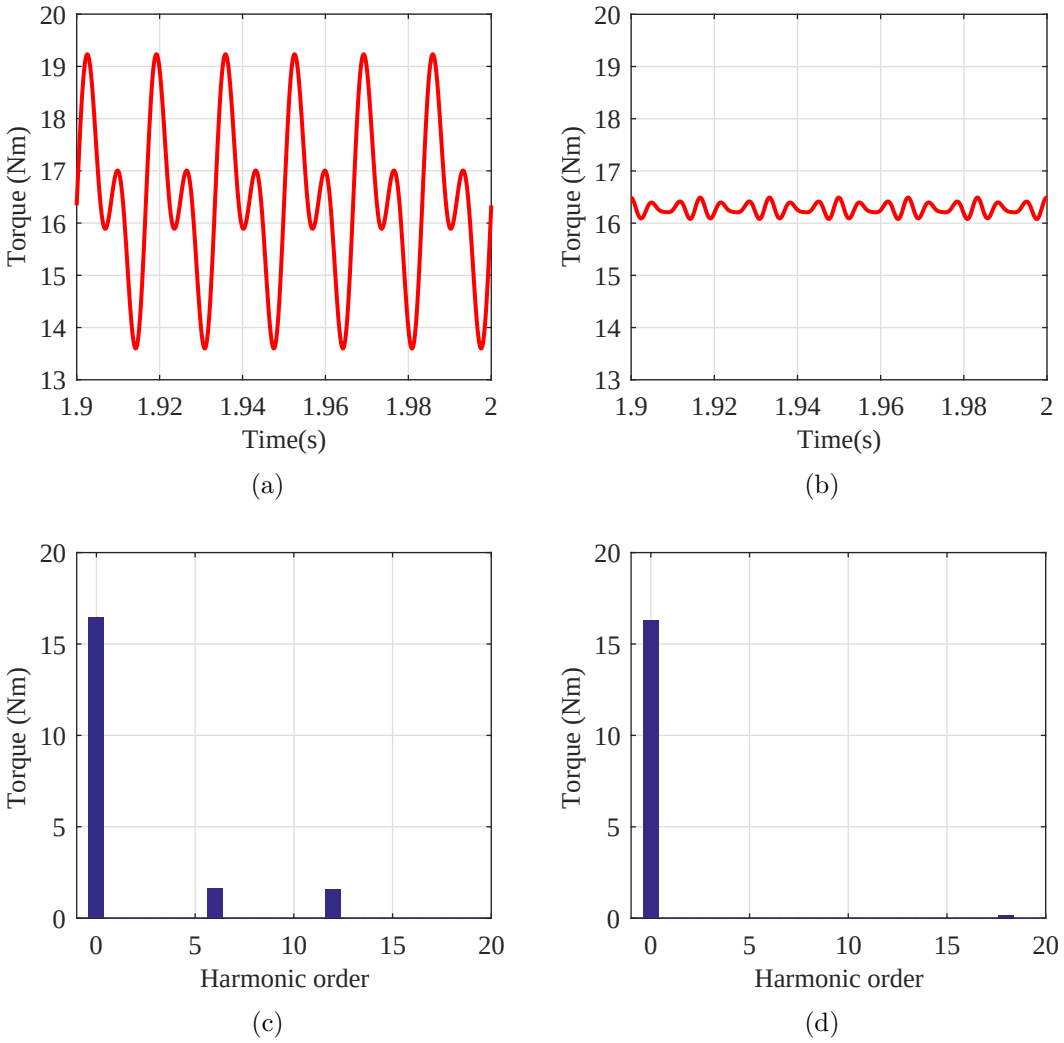

Figure 6-10: Comparison between (a) the electromagnetic torque without torque harmonic compensation and (b) the electromagnetic torque with torque harmonic compensation. (c) and (d) show the corresponding frequency spectrum.

Chapter 7

Conclusions

In order to address torque ripple and cogging torque measurements of PMSMs, an innovative rotor vibration measurement system has been developed in this Master Thesis. On the contrary of current-based techniques, the designed prototype is able to measure torque pulsation on the rotor shaft even when the machine is operating under no load conditions. By placing the prototype on the rotor shaft, direct measurements of the rotor vibration have been obtained. Tangential and radial acceleration of the shaft have been monitored through a wire-less communication interface in order to send the sampled data to an external computer. The accelerometer has been chosen according to the machine specifications in terms of sampling frequency needed, limitation of size and sensitivity.

Furthermore, the rotor vibration measurement system has been tested in a real IPMSM. Measurements of the tangential acceleration of the machine under no load conditions have been analysed. In the corresponding frequency spectra it has been observed a high-frequency harmonic with equal frequency of the theoretical cogging torque. Thus, both mathematical models and prototype have been validated. However, when the harmonic was analysed in detail, large harmonic distortion has been noticed. Therefore, a digital signal processing has been applied to the experimental results in order to estimate the mechanical speed of the machine and extract the harmonic components of the tangential acceleration in an accurate and reliable way. For the estimation of the mechanical speed, a Phase-Locked Loop (PLL) has been

implemented to carry out the gravitational acceleration tracking. The digital signal processing has been validated through FEM simulations of the machine working under different conditions. To conclude the prototype verification, a comparison of the harmonic tendency between the experimental and simulation results has been accomplished. Since approximately the same tendencies have been observed, the designed prototype has been validated.

Finally, with the aim of integrating the measurements of torque pulsation in the control strategy of the machine, a control strategy for harmonic compensation has been implemented in the simulation software, Simulink®.

Chapter 8

Future Work

There are many tests, analysis and improvements that are left to the future due to lack of time. Future work concerns deeper analysis of machine characterization and improvements to be done in the designed prototype. Some of them are stated as follows:

- Further analysis of the output torque profile in order to predict torque behaviour under different operating conditions (demagnetized magnets, overload, mechanical faults, etc.)
- Inertia and friction coefficients estimation in order to obtain torque measurement.
- Verification of machine design in terms of output torque profile.
- Improvement of the dynamic model of the IPMSM, including different aspects that can affect the performance of the machine such as eccentricities or saturation effects.
- On-line implementation of the digital signal processing to integrate the torque pulsation measurements in the control strategy of the machine.

Bibliography

[1] Bing Liu. *Fault detection of brushless permanent magnet machine drives.* PhD thesis, University of Sheffield, 2014.

[2] Thomas A Lipo. *Vector control and dynamics of AC drives*, volume 41. Oxford university press, 1996.

[3] Ben Saunders, Greg Heins, Friso De Boer, and Mark Thiele. Cogging torque estimation for sensorless pmsm. In *Electrical Machines (ICEM), 2012 XXth International Conference on*, pages 2949–2954. IEEE, 2012.

[4] Duane C Hanselman. *Brushless permanent magnet motor design*. The Writers' Collective, 2003.

[5] Matthew Piccoli and Mark Yim. Cogging torque ripple minimization via position based characterization. In *Robotics: Science and Systems*, 2014.

[6] Borja Prieto Rocandio. *Design and Analysis of Fractional-Slot Concentrated-Winding Multiphase Fault-Tolerant Permanent Magnet Synchronous Machines.* PhD thesis, Universidad de Navara., 2015.

[7] Hoang Le-Huy, Robert Perret, and Rene Feuillet. Minimization of torque ripple in brushless dc motor drives. *IEEE Transactions on industry Applications*, (4):748–755, 1986.

[8] H Jussila, P Salminen, M Niemela, and J Pyrhonen. Guidelines for designing concentrated winding fractional slot permanent magnet machines. In *Power Engineering, Energy and Electrical Drives, 2007. POWERENG 2007. International Conference on*, pages 191–194. IEEE, 2007.

[9] Nicola Bianchi and Silverio Bolognani. Design techniques for reducing the cogging torque in surface-mounted pm motors. *IEEE Transactions on Industry Applications*, 38(5):1259–1265, 2002.

[10] Xiao Ge and ZQ Zhu. Sensitivity of manufacturing tolerances on cogging torque in interior permanent magnet machines with different slot/pole number combinations. *IEEE Transactions on Industry Applications*, 2017.

[11] Dubravko Miljković. Brief review of motor current signature analysis. *HDKBR INFO Magazin*, 5(1):14–26, 2015.

[12] ZQ Zhu. A simple method for measuring cogging torque in permanent magnet machines. In *Power & Energy Society General Meeting, 2009. PES'09. IEEE*, pages 1–4. IEEE, 2009.

[13] Greg Heins, Mark Thiele, and Travis Brown. Accurate torque ripple measurement for pmsm. *IEEE Transactions on Instrumentation and Measurement*, 60(12):3868–3874, 2011.

[14] Olli Pyrhonen and Pekka Eskelinen. Advanced measurement of rotor vibration in electric drives. *IEEE aerospace and electronic systems magazine*, 13(5):21–23, 1998.

[15] Luca Ferraris, Fausto Franchini, and Emir Poskovic. The cogging torque measurement through a new validated methodology. In *Compatibility, Power Electronics and Power Engineering (CPE-POWERENG), 2017 11th IEEE International Conference on*, pages 398–403. IEEE, 2017.

[16] Analogue Devices. `http://www.analog.com/`, 8 jul 2017.

[17] NXP. `http://www.nxp.com/docs/en/data-sheet/MMA8451Q.pdf`, 10 jul 2017.

[18] C. B. Charro. *Synchronization, islanding detection and power quality improvement in distributed power generation systems.* PhD thesis, UNIVERSIDAD DE OVIEDO,Department of Electrical, Computer and Systems Engineering., 2015.

[19] W Le Roux, RG Harley, and TG Habetler. Rotor fault analysis of a permanent magnet synchronous machine. In *15th In. Conf. Elect.Mach. (ICEM'02)*. Brugge,Belgium, August 25-28, 2002.

[20] Hanju Cha, Trung-Kien Vu, and Jae-Eon Kim. Design and control of proportional-resonant controller based photovoltaic power conditioning system. In *Energy Conversion Congress and Exposition, 2009. ECCE 2009. IEEE*, pages 2198–2205. IEEE, 2009.